Top-of-Atmosphere Radiation Budget and Cloud Radiative Effects over the Tibetan Plateau and Adjacent Monsoon Regions from CMIP6 simulations

Jiandong Li[1], Zhian Sun[2], Yimin Liu[1], Qinglong You[3], Guoxing Chen[3], and Qing Bao[1]

[1]Institute of Atmospheric Physics
[2]Science to Services, Australian Bureau of Meteorology
[3]Fudan University

November 23, 2022

Abstract

This study investigates top-of-atmosphere (TOA) radiation budget (Rt) and cloud radiative effects (CREs) over the Tibetan Plateau (TP) and adjacent Asian monsoon regions including Eastern China (EC) and South Asia (SA) using the Coupled Model Intercomparison Project 6 (CMIP6) simulations. Considerable simulation biases occur but specific causes differ over these regions. Over the TP, most models underestimate the intensity of annual mean Rt and cloud radiative cooling effect, and they are hard to capture the Rt over the TP during the cold-warm transition period with the largest model uncertainty. The biases in surface air temperature and cloud fractions contribute to cloud-radiation biases over the western and eastern TP, respectively. Over EC, the intensity of Rt and cloud radiative cooling effect is seriously underestimated especially in the springtime when the model spread is large, and their biases are closely related to less low-middle cloud fractions and weaker ascending motion. Over SA, simulation biases mainly arise from longwave radiative components associated with less high cloud fraction and weaker convection, with the large model spread in the summertime. The annual cycles of Rt and CREs over EC and SA can be well reproduced by most models while the summertime peak of net CRE over the TP is later than the observation. The Rt and its simulation bias strongly depend on cloud radiative cooling effect over EC, SA, and the eastern TP. Our results demonstrate that contemporary climate models still have obvious difficulties in representing complex and various cloud-radiation processes in Asian monsoon regions.

Hosted file

`supporting_information_20201126.docx` available at https://authorea.com/users/545039/articles/601900-top-of-atmosphere-radiation-budget-and-cloud-radiative-effects-over-the-tibetan-plateau-and-adjacent-monsoon-regions-from-cmip6-simulations

Top-of-Atmosphere Radiation Budget and Cloud Radiative Effects over the Tibetan Plateau and Adjacent Monsoon Regions from CMIP6 simulations

JianDong Li[1,2], ZhiAn Sun[3], YiMin Liu[1], QingLong You[4], GuoXing Chen[4], and Qing Bao[1]

[1]*State Key Laboratory of Numerical Modeling for Atmospheric Sciences and Geophysical Fluid Dynamics, Institute of Atmospheric Physics, Chinese Academy of Sciences, Beijing, 100029*
[2]*Collaborative Innovation Center on Forecast and Evaluation of Meteorological Disasters, Nanjing University of Information Science and Technology, Nanjing, China, 210044*
[3]*Science to Services, Science and Innovation Group, Australian Bureau of Meteorology, Melbourne, Victoria, Australia*
[4]*Department of Atmospheric and Oceanic Sciences & Institute of Atmospheric Sciences, Fudan University*

Corresponding author

JianDong Li

State Key Laboratory of Numerical Modeling for Atmospheric Sciences and Geophysical Fluid Dynamics (LASG), Institute of Atmospheric Physics, Chinese Academy of Sciences

Email: lijd@mail.iap.ac.cn

Key points:

(1) Rt and cloud radiative cooling effect over the TP and EC are underestimated, but cloud radiative cooling effect is overestimated over SA.

(2) The simulated cloud-radiation biases are related to less low-middle clouds and weaker ascending motion over EC, less high clouds and weaker convection over SA, and lower surface temperature over the western TP.

(3) Most models can capture the high dependence of Rt on cloud radiative cooling effect over EC and SA, but fail to reproduce this over the TP.

Abstract

This study investigates top-of-atmosphere (TOA) radiation budget (Rt) and cloud radiative effects (CREs) over the Tibetan Plateau (TP) and adjacent Asian monsoon regions including Eastern China (EC) and South Asia (SA) using the Coupled Model Intercomparison Project 6 (CMIP6) simulations. Considerable simulation biases occur but specific causes differ over these regions. Over the TP, most models underestimate the intensity of annual mean Rt and cloud radiative cooling effect, and they are hard to capture the Rt over the TP during the cold-warm transition period with the largest model uncertainty. The biases in surface air temperature and cloud fractions contribute to cloud-radiation biases over the western and eastern TP, respectively. Over EC, the intensity of Rt and cloud radiative cooling effect is seriously underestimated especially in the springtime when the model spread is large, and their biases are closely related to less low-middle cloud fractions and weaker ascending motion. Over SA, simulation biases mainly arise from longwave radiative components associated with less high cloud fraction and weaker convection, with the large model spread in the summertime. The annual cycles of Rt and CREs over EC and SA can be well reproduced by most models while the summertime peak of net CRE over the TP is later than the observation. The Rt and its simulation bias strongly depend on cloud radiative cooling effect over EC, SA, and the eastern TP. Our results demonstrate that contemporary climate models still have obvious difficulties in representing complex and various cloud-radiation processes in Asian monsoon regions.

Key words: Tibetan Plateau; Asian monsoon regions; cloud radiative effects; radiation budget; CMIP6

1. Introduction

The Tibetan Plateau (TP), the largest and highest plateau in the world, strongly influences Asian climate and global circulation (Flohn, 1959; Li et al., 1992; Liu et al., 2020; Wang et al., 2014; Wu et al., 2007, 2015; Xu et al., 2015; Ye and Gao, 1979; Yeh, 1959). Eastern China (EC) and South Asia (SA), adjacent to the TP, possess significant Asian monsoon climate characterized by remarkable seasonal variation of circulation, precipitation and cloud fractions (Ding and Chan, 2005; Luo et al., 2009; Tao and Chen, 1987; Webster et al., 1997; Zhao et al., 2019). These three sub-regions are integral parts of the whole Asian monsoon region, and regional surface temperature, precipitation, and cloud-radiation processes are very sensitive to current climate change (Turner and Annamalai, 2012; Wang et al., 2020; You et al., 2020; Ma et al., 2021). Understanding and predicting the Asian monsoon climate are of great scientific and societal importance owing to their large impacts on a regional large population and sustainable socio-economic development. Clouds play vital roles in the earth's energy balance and the water cycle. The cloud-radiation process is one of the major uncertainties in current climate simulations and predictions (Stephens, 2005; Boucher et al., 2013; Webb et al., 2017). The reasonable projection for the TP and Asian monsoon climate therefore highly depends on an in-depth understanding of cloud-radiation processes and their improvements in climate models (Zhou et al., 2016).

Complex topography, various surface types and strong land-sea contrast are distributed in the TP and adjacent Asian monsoon regions, where circulation and cloud-radiation processes exhibit pronounced subregional features (Wu et al. 2007, 2015; Yang et al. 2014). The top-of-atmosphere (TOA) outgoing longwave radiation (OLR) over the TP is lower than adjacent low-elevation regions (Zhou et al. 2009). The compression effect from the TP topography significantly reduces cloud geometric thickness and alter its vertical structure (Luo et al. 2011; Wang et al. 2011; Yan et al. 2016). Frequent summer deep convective clouds occur in the eastern TP (Fu et al. 2020; Luo et al. 2011). EC to the east of the TP is a subtropical monsoon region, where large amounts of low-middle clouds with a strong cloud radiative cooling effect occur (Li et al., 2019; Wang et al., 2004; Yu et al., 2004). Considerable spring-summer rainfall is also distributed over EC (Ding et al. 2005; He et al. 2008; Wan and Wu, 2007). SA to the south of the TP is a tropical monsoon region, where high and strong convective clouds with large cloud water strongly reflect shortwave radiation and cause the large TOA cloud cooling (Rajeevan and Srinivasan, 2000; Saud et al., 2016). It is noteworthy that cloud-radiation characteristics over EC and SA exhibit remarkable differences, such as dominant cloud types and seasonal cycle of cloud and precipitation (Yu et al., 2001; Li et al. 2017; Luo et al. 2009; Zhang et al. 2020). These differences in cloud-radiation characteristics very likely lead to the uneven regional distribution of atmospheric radiative heating and surface-atmosphere energy over the TP and adjacent Asian monsoon regions. The uneven geographical distribution of surface-atmosphere is the basic forcing for driving atmospheric dynamics and thermal states (Trenberth et al. 2009; Webster et al. 1998). Hence, it is critical to investigate key cloud-radiation characteristics and identify their subregional differences over the TP and adjacent Asian monsoon regions for improving cloud-radiation parameterizations and reducing their uncertainties in climate models.

Although present state-of-art climate models can generally capture global distribution and intensity of major cloud-radiation properties (Dolinar et al. 2014; Flato et al., 2013; Wild et al. 2012), considerable biases in cloud-radiation simulation still exit over Asian Monsoon regions (Flato et al. 2013; Lauer and Hamilton, 2013; Li et al. 2009; Li et al. 2012; Wang et al. 2014). These biases contribute to current difficulties in simulation and prediction of Asian monsoon climate to a high degree (Boo et al. 2011; Sperber et al. 2013; Wang et al. 2020; Zhou et al. 2016). In present climate models, TOA radiation budget and cloud radiative effects (CREs) are key evaluation metrics (Flato et al. 2013). Reasonable TOA radiation budget is the basic requirement for climate models to well reproduce the climate system stability and internal feedbacks and it is strongly modulated by CREs (Trenberth et al., 2009). The CREs represent bulk cloud radiative roles in the surface-atmosphere system and are composed of longwave and shortwave CREs, with radiative cooling and warming roles, respectively (Allan, 2011; Ramanathan et al., 1987). Many climate models underestimated the intensity of cloud radiative cooling effect over EC (Wang et al. 2014; Zhang and Li, 2013) and this poor model reproducibility is partly attributed to parameterization difficulties in complex topography, cloud macro- and microphysical processes (Zhang et al., 2014; Zhou et al., 2019). The work by Li et al. (2019) showed that the spring cloud radiative cooling effect over EC is closely associated with regional ascending motion and water vapor convergence, indicating that simulation biases of cloud radiative effects are sensitive to regional circulation conditions. Notably, model evaluation studies of key cloud-radiation characteristics remain sparse for the TP and SA regions although observational analyses were conducted for the two regions (Saud et al. 2016; Yu et al., 1999; Zhao et al. 2019). Moreover, most of the existing model studies paid little attention to comparison and identification of spatial differences in CREs and TOA radiation budget and underlying influencing factors over the TP and adjacent EC and SA.

Recently, simulated data from the Coupled Model Intercomparison Project Phase 6 (CMIP6) were released (Eyring et al. 2016). Compared with previous CMIP5 data, spatial resolution and physical processes are significantly improved for climate models participating in CMIP6 (Taylor et al. 2012; Eyring et al. 2016). The CMIP6 simulation was extended to Dec. 2014 and is close to current Clouds and the Earth's Radiant Energy System (CERES) Energy Balanced and Filled (EBAF) satellite retrievals (Loeb et al. 2018), which is the most reliable TOA cloud-radiation satellite dataset so far. Thus, the comparison of CMIP6 data with CERES-EBAF satellite observations can provide a new opportunity to further evaluate and understand cloud-radiation processes over the above Asian monsoon climatic regions.

As for cloud-radiation issues over the TP and adjacent Asian monsoon regions, of the particular interests for the climatic community are (1) how well CMIP6 models reproduce spatiotemporal features of TOA radiation budget and CREs in annual mean, seasonal and interannual scales; (2) how to identify sub-regional systematic biases in the simulated TOA radiation budget and CREs and to examine the reasons for their biases; (3) try to understand the role of CREs in TOA radiation budget.

The purpose of this study is to address the abovementioned issues and provide valuable clues for understanding and improving cloud-radiation processes over the TP and adjacent Asian monsoon regions. The paper is organized as follows. Section 2 describes the data and method. Section 3 presents the simulated annual mean states. Sections 4 examine simulated seasonal and interannual variation. Section 5 analyzes the possible causes of simulation biases. Section 6 gives the conclusion and discussion.

2. Data and Methods

2.1 CMIP6 AMIP simulations

Atmospheric Model Intercomparison Project (AMIP) simulations from 27 CMIP6 models are used as model results in this study and the model information is listed in Table 1. AMIP experiment is driven by observed sea surface temperature and sea ice concentration, prescribed greenhouse gases, aerosol, solar and other forcing terms and it is designed to evaluate climate model performance and climate variability (Eyring et al. 2016). Monthly AMIP simulations range from 1979 to 2014. 9 of 27 AMIP models provide CALIPSO satellite simulator output, including total, high-, middle-, and low-cloud fraction data. There are several ensembles for each AMIP model experiments and only run 1 is used in this study.

2.2 Reference data

2.2.1 Satellite-derived data

Monthly CERES-EBAF Ed4.0 data are used to evaluate TOA radiation fluxes, CREs, and Rt (Loeb et al. 2018). These data include the TOA incident shortwave radiative flux, outgoing shortwave and longwave radiative fluxes under the clear-sky and all-sky conditions, and more details (e.g. retrieval algorithm, process methods, data uncertainties, etc.) can be referred to the CERES-EBAF website (http://ceres.larc.nasa.gov). CERES-EBAF are the most reliable dataset for TOA radiatieve fluxes and CREs to date and they are widely used as observations to measure the earth's radiation balance, cloud roles and their climatic variability. CERES-EBAF Ed4.0 data span from March 2000 to December 2018 and have a spatial resolution of 1° latitude by 1° longitude.

To better understand the simulated CREs, the general circulation model- (GCM) oriented CALIPSO Cloud data (CALIPSO-GOCCP; herein GOCCP) is used for comparison with the simulated column cloud fraction in the CMIP6 AGCMs that provide CALIPSO satellite simulator output. The GOCCP data span from June 2006 to October 2019 and include the global column total, high-, middle-, and low-cloud fractions (Chepfer et al. 2010). The GOCCP data have a horizontal resolution of 2°

latitude by 2° longitude.

2.2.2 Meteorological data

The meteorological variables to characterize the regional atmospheric circulation and surface air temperature (Ts) are obtained from the ERA-Interim reanalysis (spatial resolution of 1.0°) available from January 1979 to the present day (Dee et al., 2011). Monthly precipitation data, with a spatial resolution of 2.5°, are from the Global Precipitation Climatology Project (GPCP) (Adler et al., 2003). Despite some uncertainties, the ERA-Interim and GPCP data show very good performance in reproducing regional wind fields, atmospheric moisture, and precipitation over Asian monsoon and TP regions (Simmons et al. 2014; Huang et al. 2016). In this study, CERES satellite retrievals, ERA-Interim meteorological fields, GPCP precipitation and GOCCP data are used as observational data.

2.3 Methods

2.3.1 Definition of key concepts

The TOA radiation budget (Rt) is the difference between the TOA net incident shortwave radiation (ASR) and outward longwave radiation (OLR), and it represents the net TOA energy of the surface-atmosphere system (Trenberth et al., 2009). The intensity of Rt is highly dependent on cloud radiative roles. Generally, the net cloud radiative cooling (warming) role intensifies (weakens) the Rt intensity.

The CREs are defined as the difference in radiative fluxes at TOA between clear-sky and all-sky conditions (Allan, 2011; Ramanathan, 1987), and includes longwave and shortwave cloud radiative effects (herein, LWCRE and SWCRE). The net CRE (NCRE) is the arithmetic sum of LWCRE and SWCRE. These terms effectively measure the bulk role of clouds in the atmosphere–surface system and are therefore widely used in researches on model evaluation, climatic variability, and uncertainties (Boucher et al. 2013).

Note that the sign of SWCRE is negative and its increase denotes the SWCRE intensity weakens. The same applies to NCRE except for high surface albedo regions. The abbreviations of the variable names used in this study are listed in Table 2.

2.3.2 Evaluation metrics

To evaluate the climatological states of CMIP6 simulations, statistical metrics including domain overall mean (bias), relative bias, spatial (pattern) temporal correlation, standard deviation and root-mean-square error (RMSE) are used to represent model reproducibility compared with observed states. These statistical metrics are commonly used in model assessment (Pincus et al. 2008; Taylor, 2001; Wang et al. 2014), and their use and formulas are listed in supplementary materials. To clearly and simply represent simulation skills of CMIP6 AMIP models, we used a simplified square Taylor diagram to quantitatively show simulated spatial similarity and biases, and the model spread degree.

In this study, the 500-hPa vertical velocity and Ts from CMIP6 simulations are compared to ERA-Interim data to understand the effects of atmospheric convection and surface thermal state on CREs and Rt.

2.3.3 Data treatment

The observational and simulated data during 2001-2014 are extracted to analyze climatological annual mean, seasonal and interannual variation. GOCCP and corresponding model data during 2007-2014 are used to investigate simulated biases of cloud fractions and CREs. The run one in each model AMIP ensemble is selected. The multi-model ensemble (MME) is based on the equal-weighted average of individual models. To obtain MME and facilitate the inter-comparison among models, AMIP simulations are regridded into a common horizontal resolution of 1.0° latitude by 1.25° longitude via bilinear interpolation.

In this study, the domain of TP is specified as 27.5-37.5°N and 80-100°E, and adjacent East China (EC) and South Asia (SA) monsoon regions are set in an area of 22-32°N and 102-122°E, and 15.5-25.5°N and 80-100°E, respectively (Figure 1c).

3. Annual mean states

3.1 Observational states

3.1.1 Geographical distribution of annual mean cloud-radiation variables

Figure 1 presents the global distribution of annual mean Rt. The zonal variation of Rt is small in the Southern Hemisphere but large in the Northern Hemisphere due to its larger land area and more complex topography. The large NCRE is mainly located in the Pacific and Atlantic stratus regions, mid-latitude storm track regions, EC, and South Ocean. The Rt in most parts of the TP is up to 10 W m^{-2} and is the strongest positive Rt in land area of the same latitude (Figure 1a). Over the TP, the OLR and Ts (not shown) are obviously lower relative to adjacent regions (Figure 2b). Subtropical EC lies in downstream of the TP, with a negative Rt from −40 to −20 W m^{-2} and the largest cloud radiative cooling effect up to −60 W m^{-2} at the same latitudes (Figures 1a-1b). Over EC and south flank of the TP, the strong negative Rt coincide with large ASR, TCF and NCRE (SWCRE) (Figures 1b, 2a, 2d, 2e, 2f), indicating that regional Rt is strongly related to cloud radiative cooling role in the two regions. South Asian regions to south of the TP are tropical monsoon regions where the obvious positive Rt and negative NCRE occur. Although there is considerable amount of TCF, the offset between LWCRE and SWCRE makes the intensity of NCRE over SA and the TP weaker than that over EC (Figures 1b, 2d, 2e, 2f). Over SA, the TOA net incident shortwave radiation (ASR) is larger than those over EC and TP due to lower latitude (Figure 2a). These results demonstrate that pronounced sub-regional differences of cloud-radiation features over the TP and adjacent Asian monsoon regions.

3.1.2 Domain-averaged values of TOA cloud-radiation variables

Table 3 lists annual mean values of domain average TOA radiative fluxes and CREs. The annual mean Rt over EC, SA and the TP are −12.0, 28.8 and 7.7 W m^{-2}, respectively. The ASR over EC and the TP are 228.0 and 231.6 W m^{-2}, respectively, and their differences are not large. The TP latitude is the highest but its TOA incident shortwave radiation is the lowest among these three regions. The OLR over the TP is 220.3 W m^{-2} and is much lower than those over EC (243.8 W m^{-2}) and SA (253.1 W m^{-2}). The relatively lower OLR over the TP is directly responsible for its positive Rt. The upward shortwave radiation, SWCRE and NCRE over EC are 142.3, −83.2 and −48.5 W m^{-2}, respectively, and their intensity is much larger than the counterparts over SA and the TP. Given the close spatial pattern shown above, the significant negative Rt over EC is caused by its strong shortwave cloud radiative cooling effect to a large extent.

3.2 Simulated annual mean states

3.2.1 Simulated annual mean states of Rt

Figure 3 shows the geographical distribution of annual mean Rt simulated from CMIP6 AMIP models. Over the TP, most models can capture the Rt distribution, especially positive Rt vaule over the central and eastern TP and negative Rt value over the south flank of the TP, but somewhat underestimate the Rt over the western TP (Figure 3bb). The regional mean biases of Rt, ASR and OLR in MME are −4.0, −10.2 and −6.1 W m^{-2}, respectively, and their pattern correlation coefficients (PCCs) are 0.48, 0.66 and 0.94, respectively (Table 4). This shows that ASR is mainly responsible for regional mean bias and spatial pattern of Rt in many models. Particularly, the seriously underestimated Rt over the western TP is directly linked to the same underestimated ASR in CanESM5, CNRM-CM6-1, CNRM-ESM2-1, FGOALS-g3, and MIROC6, and their PCCs are less than 0.2 over the TP (Figure 5h).

Over EC, most models can roughly represent the spatial pattern of Rt but seriously underestimate its magnitude (Figure 3bb). The regional mean Rt in MME over EC is 1.0 W m^{-2} and its intensity is much lower than the observational value of −12.0 W m^{-2} (Figure 4a). As listed in Table 4, the regional mean value and RB of ASR in MME over EC are 14.8 W m^{-2} and 6.4%, respectively, and much larger than the counterparts (1.8 W m^{-2} and 0.7%) of OLR. This indicates that the simulated weaker Rt is mainly attributed to the obviously underestimated ASR. Over EC, regional mean Rt in ACCESS-ESM1-5 (−14.0 W m^{-2}), CAMS-CSM1-0 (−7.4 W m^{-2}), GISS-E2-1-G (−16.4 W m^{-2}), and MRI-ESM2-0 (−14.3 W m^{-2}) are relatively close to the observation and their absolute RBs are less than 40% (Figure 4a). Meanwhile, these four models also reproduced well the regional mean ASR over EC, with absolute RBs less than 30% (Figure 4b). ACCESS-ESM1-5 (0.81), CanESM5 (0.80) and CESM2 (0.81) have higher PCCs of Rt than MME (0.76) (Figure 5a). Note that the sign of regional mean Rt over EC in CanESM5 and BCC-ESM1 is positive, suggesting that the two models actually can't reasonably represent Rt over EC (Figure 4a). The PCCs of Rt in FGOALS-g3 and IPSL-CM6A-LR are only 0.17 and −0.02, respectively, and they even produced evident positive Rt over EC (Figures 3m and 3s), which are caused by their larger biases and poor spatial reproducibility of ASR (Figure 5b). This further demonstrates that the spatial pattern of Rt in these AMIP models is mainly related to that of the simulated ASR.

Over SA, most models can reproduce the positive Rt although the simulated Rt intensity is weaker than the observation (Figure 3bb), with regional mean Rt and RB in MME are 25.2 W m^{-2} and −10% (Table 4), respectively. Most models can reproduce well the spatial patterns of Rt and ASR over SA, with PCCs over 0.7 (Figure 5e). The regional mean biases of ASR and OLR in MME are 0.6 and 3.4 W m^{-2} (Table 4), respectively, showing the underestimated Rt over SA is mainly caused by the overestimated OLR. The PCC of OLR in MME is 0.83, which is lower than the ASR (0.95) and Rt (0.94) over SA (Table 4). The low PCCs of OLR in some models (e.g. ACCESS-ESM1-5, E3SM-1-0, HadGEM3-GC31-LL, MPI-ESM1-2-HR) are less than 0.4 (Figure 5f) and their poor reproducibility may be related to their unreasonable location of the tropical strong convection over SA.

Note that the PCCs of Rt and its shortwave and longwave components in MME are clearly higher than those in individual models over the above three regions (Figure 5).

3.2.2 Simulated annual mean states of CREs

Figure 6 shows that the geographical distribution of annual mean NCRE simulated from CMIP6 AMIP models. Over the TP, most models can reproduce the large NCRE over the eastern TP and south flank of the TP (Figure 6bb). Most models can represent well the spatial pattern of NCRE (SWCRE) (Figure 6), with the PCC of 0.87 (0.92) in MME (Figures 8g-8h), but have relatively worse reproducibility for LWCRE, with the PCC of 0.61 in MME (Figure 8i). Most models underestimate the NCRE intensity, especially over the western TP (Figure 6bb), and the regional mean NCRE in MME is −17.5 W m^{-2} (Figure 7g). The regional mean biases of NCRE, SWCRE and LWCRE in MME over the TP are 7.2, 11.2 and −4.0 W m^{-2} (Table 4), respectively, suggesting the weak simulated NCRE still arises mainly from underestimated SWCRE. By comparison, ACCESS-CM2, HadGEM3-GC31-LL, HadGEM3-GC31-MM, and UKESM1-0-LL have better simulation skills of CREs regarding their PCCs and RMSEs.

Over EC, most models can represent large negative NCRE, but obviously underestimated the NCRE intensity (Figure 6bb). The regional mean value of NCRE in MME is −37.1 W m^{-2} averaged over EC and much lower than the observation (−48.6 W m^{-2}) (Figure 7a). Many models fail to capture the regional center of NCRE over southeastern China (Figure 6bb), resulting in their poor PCCs of NCRE (Figure 8a), and the PCC of NCRE in MME is 0.59 (Table 4). Because the NCRE over EC is dominated by SWCRE, the spatial pattern and PCCs of simulated NCRE in models are very similar to their individual SWCRE (Figure 8a). As shown in Figures 7b-7c and Table 4, the regional mean biases of SWCRE and LWCRE in MME are 22.0 W m^{-2} and −10.5 W m^{-2} averaged over EC, respectively, and the magnitude of both SWCRE and LWCRE is obviously underestimated. This demonstrates that SWCRE dominates not only the sign of NCRE but also accounts for the bias intensity of NCRE over EC. The PCCs of SWCRE and LWCRE in MME are 0.52 and 0.31 over EC, respectively (Table 4). The PCCs of NCRE in CESM2, ACCESS-ESM1-5, MRI-ESM2-0, MPI-ESM1-2-HR, and NESM3 are larger than MME (Figure 8a), and these models can capture the regional center of NCRE over southeastern China (Figure 6). Compared to other models, CESM2 and MPI-ESM1-2-HR can reproduce better NCRE over EC (Figure 6), with the SPCs of 0.73 and 0.67, respectively (Figure 8a).

Over SA, unlike to EC and the TP, most models overestimate the intensity of cloud radiative cooling effect (Figure 6bb), and the regional mean NCRE in MME, with a value of −18.6 W m^{-2}, is stronger than the observation (−12.3 W m^{-2}) (Figure 7d; Table 4). The overestimated NCRE is mainly attributed to the underestimated LWCRE. As listed in Table 4, regional mean biases of SWCRE and LWCRE in MME are 2.9 and

−9.3 W m^{-2} averaged over SA, respectively. Most models can reproduce the spatial pattern of NCRE (LWCRE and SWCRE) over SA (Figures 8d, 8e, 8f; Table 4). The PCCs of NCRE, LWCRE and SWCRE in MME are 0.74, 0.75 and 0.77, respectively, which are very close to each other (Table 4). CESM2 and NorESM2-LM have relatively better performances in the spatial pattern and intensity of NCRE, SWCRE, and LWCRE over SA.

The MME can substantially improve simulated Rt and NCRE, and their longwave and shortwave counterparts, especially for their spatial distribution. The PCCs of Rt, ASR and OLR (NCRE, SWCRE and LWCRE) of MME are higher than most individual models (Figures 5a, 5d, 5g, 8a, 8d, 8g). In Figures 5 and 8, the center RMSE is used to measure the spatial pattern biases and the spread degree of grids shows the spread degree of multi-model results. The model spreads of Rt and ASR over the TP are much larger than the counterparts over EC and SA (Figures 5a, 5d, 5g). The model spreads of NCRE and SWCRE are relatively larger over EC and SA. Notice that the spread pattern of simulated Rt (NCRE) is very close to that of ASR (SWCRE) in EC and the TP (Figures 5a-5b, 5g-5h, 8a-8b, 8g-8h), where the ASR (SWCRE) bias mainly accounts for the Rt (NCRE) bias. This similar bias distribution further indicates the dominant role of the shortwave component in the simulation biases of TOA Rt (CREs) over EC and the TP regions. Moreover, the spread degree of OLR (LWCRE) is very large over SA (Figures 5f and 8f), reflecting that various simulated convection intensity and distribution occur in CMIP6 AMIP models. Note that despite of the absolute contribution of LWCRE to NCRE is relatively smaller over SA (Table 4), the spread degree of simulated LWCRE is very large over EC, where current climate models probably have big differences in reproducing cloud height and cloud vertical distribution (Zhang and Jing, 2016).

It is noteworthy that ACCESS-CM2 and its coupled counterpart (ACCESS-ESM1-5) show some differences in the spatial pattern and intensity of NCRE over EC (Figures 6a, 6b, 7a). These simulation differences are very likely caused by different parameters setting in physical processes. Compared with their respective high resolution versions (CNRM-CM6-1-HR and HadGEM3-GC31-MM), CNRM-CM6-1 and HadGEM3-GC31-LL with lower resolution have similar performances in spatial patterns of Rt and NCRE over the above three regions. Over EC, the PCCs of Rt and NCRE in HadGEM3-GC31-MM are 0.71 and 0.53, respectively, and higher than the counterparts (0.55 and 0.40) in HadGEM3-GC31-LL (Figures 5a and 8a). Over the TP, the PCCs of Rt and NCRE in HadGEM3-GC31-MM are 0.90 and 0.72, respectively, and are higher than those (0.86 and 0.43) in HadGEM3-GC31-LL (Figures 5g and 8g). This demonstrates that some high resolution models have better performance with the improvement of fine-topography and relevant sub-grid cloud processes (Haarsma et al. 2016).

4. Annual cycle and interannual variation

4.1 Observational annual cycle

Figures S1 show observational annual cycles of regional mean Rt, NCRE and their individual shortwave and longwave components averaged over three regions. The positive Rt over SA and the TP first occurs in March and over EC in April, and then the positive Rt stay until September over EC and the TP, and October over SA (Figure S1a). The Rt value over SA is larger than those over EC and the TP in most months except for July and August (Figure S1a). It is noteworthy that the sensible heating over the TP becomes positive from March onward and stays until October (Wu et al., 2007). The similar duration time between Rt and surface sensible heating also indicates surface states are key influencing factors to regional Rt over the TP. The seasonal variation range of OLR over EC and the TP is much weaker than that over SA (Figure S1c). The intensity of NCRE and SWCRE over EC are much larger than those over SA and TP in most months, especially in December-March (Figures S1d and S1e) when large amounts of low-middle clouds occur (Pan et al. 2015; Li et al. 2017). Over SA, the maximum Rt (ASR) intensity occurs in May (April) when it is before the monsoon onset month (June), and the intensity of CREs (NCRE, SWCRE and LWCRE) peak in July when the summer monsoon erupts (Figures S1a and S1d-S1f). Compared with May, the convection intensity and cloud fractions increase quickly but the intensity of ASR and OLR decrease over SA in June and July (summer monsoon period) when convection and CREs become stronger than those before the monsoon onset (Zhang et al. 2020).

4.2 Simulated annual cycle

4.2.1 Simulated annual cycle of Rt

Figure 9 shows the simulated annual cycles of Rt, ASR, and OLR averaged over three regions. Over the TP, most models overestimate the negative Rt from December to February but simulate well the Rt intensity from May to November (Figure 9g). Notably, most models and MME can't reproduce the positive RT in March (Figure 9g). Nonetheless, several models including ACCESS-CM2, HadGEM3-GC31-MM, and UKESM1-0-LL can success to reproduce the positive Rt over TP in March and its annual cycle (Figure S2a), and their RMSEs of Rt annual cycle are much smaller than other models (Figure 10a). By comparison, the simulation bias and model spread of Rt over the TP mainly contributed by the ASR are larger from February to May than those over EC and SA (Figures 9g-9i and 10g-10i), indicating that the model uncertainty of

Rt is very large during the cold-warm transition period over the TP. In the meantime, the large range of ASR and OLR over the TP from May to June exhibit the large impact of summer monsoon on simulated TOA radiation (Figures 9h-9i).

Over EC, most models can capture well seasonal ranges of Rt and ASR and their peaks in July (Figures 9a-9b), and their PCCs of Rt and ASR are over 0.97 (Figures 10a-10b). However, most models underestimate the Rt intensity from October to February and overestimate it from April to August (Figures 9a-9b). The ASR intensity over EC is underestimated by most models in the whole year while the annual cycle of simulated OLR is very close to the observation (Figures 9b-9c). Compared to other models, GFDL-AM4 and MRI-ESM2-0 have better simulation skills in the PCC and RMSE of Rt over EC (Figures 10a-10c). Moreover, the similar spread pattern between Rt and ASR shows that the Rt bias and its model spread over EC is dominated by the ASR (Figures 9a-9b and 10a-10b).

Over SA, most models simulate well annual cycles of Rt, ASR and OLR, and can capture the peak of Rt (ASR) in May (April) and the valley of OLR in July (Figures 9d-9f). Most models overestimate the intensity of ASR and OLR over SA from May to September, and the model spread of ASR and OLR and their biases are very large from May to June (Figures 9e-9f and 10e-10f). Over SA, the ASR intensity is underestimated from November to April and the OLR is systematically underestimated by the models in the whole year although seasonal ranges of ASR and OLR are well captured by models (Figures 9e-9f). Based on simulation skills of PCC and RMSE, CESM2, GFDL-AM4 and NorES2-LM are better at Rt over SA.

4.2.2 Simulated annual cycle of CREs

Figure 11 shows the simulated annual cycle of NCRE and its longwave and shortwave components. Over the TP, most models underestimate LWCRE and SWCRE from January to July, and NCRE from February to May (Figures 11g-11i). The offset between LWCRE and SWCRE over SA makes the simulated NCRE in MME peaks in July while it is June in the observation. NorESM2-LM can capture the NCRE peak in June over the TP and it has the highest PCC (0.9734) and the smallest RMSE (Figure 12g) in all models. HadGEM3-GC31-LL, HadGEM3-GC31-MM and CESM2 also have better reproducibility in the NCRE over the TP (Figure 12g). The model spread of NCRE is relatively larger in summertime (Figure 11a, 11d, 11g).

Over EC, models basically simulate large NCRE from February to May, but obviously underestimate its intensity in most months (Figure 12a). The underestimation of the intensity of NCRE and Rt exist simultaneously over EC. As shown in Figures 11d and 11g, the systematic underestimation of simulated LWCRE and SWCRE appears in the whole year, and the magnitude of underestimated SWCRE is larger than LWCRE expect for July and August when the NCRE in MME is relatively close to the observation. Relatively, MPI-ESM1-2-HR and NorESM2-LM perform better in the NCRE intensity from February to May and its annual cycle relative to other models (Figures 11a and 12a).

Over SA, most models can capture well the peaks of NCRE, LWCRE and SWCRE in July, but underestimate the LWCRE intensity especially from May to October (Figures 11d-11f), indicating that the convection is also weaker compared to the observation. Due to the strong offset between LWCRE and SWCRE biases in the summertime, the simulated NCRE bias over SA is smaller than its longwave and shortwave components. Particularly, ACCESS-ESM1-5 simulates an opposite annual cycle of the NCRE phase relative to the observation (Figure 12e), which is mainly caused by its weaker SWCRE during November-March and summer time (not shown). Moreover, HadGEM3-GC31-LL, HadGEM3-GC31-MM, and UKESM1-0-LL also have weaker SWCRE and NCRE in summer (Figure 12e). The model spread of simulated CREs and their biases over SA, especially for biases of NCRE and SWCRE, is very large from May to September (Figures 11d-11f).

The results mentioned above show that the large model spread of the simulated NCRE and SWCRE over EC occurs during the springtime, and the counterparts over SA are during the summertime. In the same period, large amounts of dominant low-middle and high clouds occur over EC and SA, respectively, and correspond to their strong NCRE and SWCRE. In addition, the intensity of simulated LWCRE and SWCRE and their ratios directly determine whether the NCRE intensity and its annual cycle over SA are reasonable in these models. Thus, current CMIP6 AMIP models still face considerable uncertainties in reproducing the intensity of TOA CREs in their peak months over the TP and adjacent monsoon regions.

4.3 Interannual variation

4.3.1 Simulated time series of Rt and NCRE

Table 5 lists interannual variation of simulated Rt and NCRE during 2001-2014. Here, the STD is used to represent the intensity of interannual variation. There is pronounced interannual variation for Rt and NCRE over three regions. The STDs of observational Rt and NCRE over the TP are 3.64 and 4.67 W m^{-2}, respectively, and the counterparts over SA are 4.19 and 3.72 W m^{-2}, respectively. The STDs of observational Rt and NCRE over EC, with values of 7.76 and 8.53 W m^{-2}, respectively, are almost twice larger than the counterparts over SA and the TP (Table 5), indicating larger interannual variation over EC. Compared with the observation and individual models, the magnitude of interannual variation of Rt and NCRE weakens substantially in MME and most models are hard to capture well the interannual variations of Rt and NCRE, only with the temporal correlation coefficients less than 0.2 in MME. By comparison, models have better interannual reproducibility over EC, with temporal correlation coefficients of 0.19 and 0.20 for Rt and NCRE in MME, respectively, but the counterparts in MME are much lower over SA and the TP (not shown).

4.3.2 Interannual relationship between NCRE and Rt

To examine the potential role of NCRE in Rt, Table 5 shows the temporal correlation between monthly NCRE and Rt averaged over three regions during 2001-2014. Over EC, the correlation coefficients between NCRE and Rt in the observation and MME are 0.93 and 0.88, respectively, and the temporal correlation coefficients in most models are close to or over 0.85. This demonstrates the interannual variation of Rt can be well explained by the NCRE. Over SA, the observed and simulated correlation coefficients between Rt and NCRE are 0.73 and 0.71, respectively. Over the TP, although the observed correlation coefficient between Rt and NCRE is 0.75, the simulated counterpart is only 0.42. The model spread of correlation coefficients over the TP is larger than those over EC and SA, and the coefficients in CNRM-CM6-1 and CNRM-ESM2-1 are even less than 0 (not shown). The interannual relationships between Rt and NCRE demonstrate that cloud radiative roles have the dominant role in the Rt variation over EC and SA, and models can well represent this relationship, especially over EC. However, the observed large contribution of cloud to Rt can't be simulated well in most CMIP6 AMIP models. This means that other factors, such as surface states, also have certain effects on Rt over the TP.

5. Possible causes for simulation biases

In this section, we investigate possible causes for simulation biases of Rt and CREs in CMIP6 models over the TP and adjacent EC and SA. The spatial distribution of simulation biases of cloud-radiation variables is analyzed first, and the relationship between simulated Rt and CREs biases is examined to highlight cloud roles in simulated Rt biases. CREs are closely related to cloud fractions being very sensitive to regional circulation conditions and surface states. We further examine the influences of simulated cloud fractions on CREs and potential associations between simulated cloud fraction and meteorological conditions.

5.1 Geographical distribution of simulation biases

Figure 13 shows the geographical distribution of simulated biases of Rt, NCRE, and relevant radiative fluxes in MME. Over the central TP and south flank of TP, positive Rt bias corresponds to negative biases ASR and RSUT, and positive NCRE (SWCRE) bias, suggesting an overall underestimated cloud radiative cooling effect. Over the western TP, negative Rt bias is coincident with negative biases of ASR and OLR and positive biases of RSUT (RSUTCS) and NCRE (SWCRE). The cloud-radiation biases exhibit an obvious difference between the western and eastern TP. In this case, the PCC between NCRE (SWCRE) and Rt biases is only 0.27 (0.36) over the TP (Figure S3g and S3h), indicating that cloud biases are not responsible for the Rt bias over the whole TP. The similar spatial pattern among the biases of Rt, RSUT (RSUTCS), OLR (OLRCS), and NCRE (SWCRE) suggest the surface state biases (e.g. surface temperature and albedo) may strongly contribute to cloud-radiation biases over the western TP.

Over EC, clear positive Rt bias coincides with negative RSUT biases and positive biases of ASR and NCRE (SWCRE), and their maximum biases centers nearly occur over southwestern China. As mentioned above, the LWCRE intensity over EC is underestimated (Figure 13i). The PCC between the biases of NCRE (SWCRE) and Rt is up to 0.93 (0.88) over EC, but the counterpart between LWCRE and Rt is only 0.18 (Figure S3c). This demonstrates that the seriously underestimated negative Rt over EC highly depends on cloud biases in CMIP6 AMIP models, especially the underestimated cloud radiative cooling effect (SWCRE).

Over SA, the LWCRE intensity is underestimated in the whole region (Figure 13i). Note that the spatial pattern of Rt bias is also similar to those of NCRE and SWCRE in the Bay of Bagel (BOB), southern India, and Indochina Peninsula (Figure 13a, 13g, 13h). The PCC between Rt and NCRE biases is 0.85 (Figure S3d), and the PCC between SWCRE (LWCRE) and Rt biases is 0.63 (0.41) over SA (Figures S3e-S3f). The high spatial correlation suggests that cloud biases account for the Rt bias to a large extent. In addition, the strong CREs and their longwave and shortwave components often coexist with strong convective activities over SA (Hartmann et al., 2001; Kiehl, 1994; Li et al., 2017; Rajeevan and Srinivasan, 2000). Thus, although the underestimated domain-mean positive Rt over SA mainly arises from its underestimated cloud warming effect (LWCRE), the spatial pattern bias of Rt is sensitive to regional SWCRE biases in the BOB where strong convection happens frequently.

5.2 Simulation biases of cloud fractions

Figures S4 and S5 shows the geographical distribution of simulated TCF and HCF in 9 models with satellite simulator output, respectively. In the observation, large amounts of cloud fractions occur over EC (Figure S4k and 14a), especially over southeastern China, and low-middle clouds account for a large proportion of total clouds (Pan et al. 2015; Li et al. 2017). Low-middle clouds mainly consisting of liquid water can strongly reflect incident shortwave radiation and cause large SWCRE and

NCRE (Figures 15a-15b) over EC (Li et al. 2017, 2019). Lots of high clouds prevail over the eastern TP and SA (Figures S5, 14e, 14f) especially in summer, which lead to certain intensity of LWCRE and SWCRE (Figures 15b-15c).

In the simulation, most models seriously underestimate annual mean TCF and high cloud fraction (HCF) over EC, SA and most parts of the TP (Figures 15a-15f). Particularly, MCF and LCF simulated by most modes are lower than the observation over EC (not shown), where TCF and HCF in the whole year are almost underestimated (Figures 14a and 14d). The underestimated TCF over EC coincides well with the identically underestimated SWCRE and NCRE (Figures 15d-15e, 15g). The PCC between NCRE (SWCRE) and TCF biases in the MME is −0.78 (−0.83) over EC (Figures S6a-S6b). This good correspondence relationship between TCF and SWCRE (NCRE) biases demonstrates that less cloud fractions directly result in the underestimated intensity of cloud radiative cooling effect over EC. The underestimated LWCRE in annual mean MME corresponds to less HCF over EC and SA (Figures 15f and 15i). The correlation coefficients between HCF and LWCRE biases in annual mean MME are 0.53 and 0.47 over EC and SA, respectively (Figures S6c and S6f), indicating that LWCRE bias highly relies on HCF biases in CMIP6 models.

Over the TP, the underestimated TCF and HCF mainly appear from January to August (Figures 14c and 14f), when underestimated SWCRE and LWCRE also occur. In addition, the phenomena that late peak month (July) of NCRE in MME mainly occur in the western TP and is caused by obviously underestimated LWCRE (not shown). As shown in Figures S4 and S5, TCF and HCF are larger over the eastern TP than those over the western TP (Bao et al. 2019), and therefore clouds exert more influences on the intensity of CREs and their biases over the eastern TP. The correlation coefficients between TCF (HCF) and SWCRE (LWCRE) is −0.24 (0.39), and significantly higher than the counterparts over the whole TP (Figures S6h and S6i).

As for individual models, those models with better-simulated column CFs can better simulate CREs. For instance, CESM2 and UKESM1-0-LL well reproduce LCF over EC and HCF over the eastern TP, and they can also well capture the intensity and spatial pattern of regional SWCRE and LWCRE (not shown).

5.3 Simulation biases of meteorological conditions

The formation and maintenance of cloud fractions highly rely on regional meteorological conditions, especially ascending motion. Figure 16 shows observational wind fields, surface skin temperature, and their simulation biases in the aforementioned 9 models. We use 500-hPa vertical velocity to represent the whole atmospheric vertical motion. The strong ascending motion occurs over maritime continents, the southern and eastern BOB, eastern TP and EC (Figure 16a). The low-level southwestern wind from the BOB reaches into EC and the eastern TP, and the southern wind east to the west Pacific anti-cycle also comes into EC from the South China Sea. Thus, considerable amounts of water vapor are transported into the eastern TP and EC (Figure 16a) and is provided as cloud water sources. In the meantime, EC is just located in the south of 200-hPa westerly jet entrance, which is favorable to maintain regional low-middle ascending motion and large SWCRE (Liang and Wang, 1998; Li et al. 2019).

Compared with the observations, obvious weaker ascending motion lies in maritime continents, the southern BOB and the TP, and this bias inhibits strong convection and formation of HCF (Figures 15i and 16c). Large positive Ts bias occurs over the Indian and continents east and north to the BOB, Indochina Peninsula and EC while Ts bias is very small over ocean regions (Figure 16d). Thus, the easterly (northerly) wind-induced by simulated biases in regional thermal-dynamical distribution is not conducive to the ascending motion over the eastern BOB (Figure 16c). As a result, HCF and LWCRE are underestimated over these regions (Figures 15f and 15i). There is a large negative Ts bias (surface cooling) over the western TP and just corresponds to the underestimated OLR and underestimated RSUT (Figures 13c-13d and 15d). The simulated lower Ts over the western TP is generally related to surface state biases in models, especially overestimated surface albedo (Chen et al. 2017). There is an obvious weaker 200-hPa westerly jet between the eastern TP and EC (Figure 16c), which can suppress the ascending motion south to these regions. The simulated weaker low-middle ascending motion doesn't benefit to the formation and maintenance of regional low-middle CFs over EC, and then causes underestimated the intensity of regional SWCRE and NCRE (Li et al., 2019, 2020). Moreover, Note that stronger ascending motion occurs in MME over western EC, where weaker SWCRE (NCRE) intensity still appears (Figures 15d-15e and 16c). Over western EC and the eastern TP where the topography is very complex, sub-grid atmospheric states and diurnal cloud variation are hard to be reproduced in models (Zhang et al. 2014; Chen and Wang, 2016), and observational Ts and column cloud fraction data remain large uncertain (Chen and Frauenfeld, 2014; Fu et al. 2020; Wang and Zeng, 2012). In addition, AMIP-like model run forced by observational sea surface temperature instead of simulated counterparts probably gives rise to unreasonable regional air-sea interactions (Sperber et al., 2013), and may induce simulation biases of westerly jet or land-sea Ts contrast exist over Asian monsoon regions.

Another notable issue is the simulated aerosol-radiation-cloud biases in contemporary models. Heavy aerosol loading is distributed in EC, where cloud radius and optical depth are very sensitive to aerosols (Li et al. 2016; Wu et al., 2016). Many climate models obviously underestimated the aerosol loading and optical depth over

EC (Li et al., 2014; Shindell et al., 2013). The weaker simulated aerosol optical depth can lead to weaker upward shortwave radiation at the TOA and also added large uncertainties into cloud radiative properties and lifetime. Since the outputs of CMIP6 AMIP models do not include these variables associated with the cloud-aerosol interaction, detailed analysis cannot be done in this study.

6. Summary and discussion

This study examined TOA Rt and CREs over the TP and adjacent Asian monsoon regions in CMIP6 AMIP simulations. Our results show that specific model performances vary over the TP and adjacent EC and SA.

Over the TP, most models roughly represent the distribution of Rt and NCRE but underestimate their intensity. These biases of Rt and NCRE mainly arise from their underestimated shortwave components (ASR and SWCRE). The simulated spatial reproducibility of annual mean Rt over the TP is quite lower, with a spatial correlation of 0.48 in the MME. The simulation bias and model spread of Rt over the TP are larger from February to May, indicating that the simulation uncertainty of Rt is quite large during the cold-warm transition period. Most models fail to reproduce the positive RT value over the TP in March, except for UKESM1-0-LL, ACCESS-CM2, and HadGEM3-GC31-MM. Although NorESM2-LM, HadGEM3-GC31-LL, HadGEM3-GC31-MM, and CESM2 can success to capture the peak month (June) of NCRE over the TP, most models produce a late NCRE peak in July relative to the observation. This late NCRE peak month in CMIP6 simulations is more obvious in the western TP.

Over EC, most models seriously underestimate the annual mean intensity of Rt and NCRE, especially over southwestern EC. The underestimated intensity of Rt is mainly caused by the overestimated ASR. Cloud radiative cooling effect dominated by

SWCRE over EC is seriously underestimated by most models from February to May when the large model spread also occurs. Only several models (e.g. ACCESS-ESM1-5, CESM2, GFDL-AM4, and MPI-ESM1-2-HR) can reasonably capture the spatial pattern and intensity of Rt (NCRE) over EC, but most models are still hard to reproduce the intensity center of NCRE (SWCRE) over southeastern EC.

Over SA, most models can represent well the spatial distribution of Rt and NCRE. In contrast to EC and the TP, the biases of Rt and NCRE are mainly caused by their longwave components. The overestimated (underestimated) OLR (LWCRE) largely accounts for the underestimated (overestimated) intensity of Rt (cloud radiative cooling effect) in CMIP6 models over SA. The largest model spread of CREs occurs especially from May to September. By comparison, most models can capture well the peak months of Rt and CREs over SA.

The MME in CMIP6 models can improve simulated spatial similarity and biases of Rt, NCRE, and their components over the TP and adjacent monsoon regions for annual mean and seasonal variation states. Even so, most models are hard to capture well the interannual variations of Rt and NCRE over the above three regions, with quite low monthly temporal correlations with the observations, and underestimate the intern-annual intensity of NCRE and Rt over EC. Most models can reproduce well the close interannual relationship between observational NCRE and Rt over EC and SA, especially in the former, further suggesting that vital cloud radiative roles in the TOA Rt. However, the majorities of models show very low reproducibility in this interannual relationship over the TP, except for ACCESS-CM2, ACCESS-ESM1-5, MPI-ESM1-2-HR, and UKESM1-0-LL.

It is noteworthy that no one model has the best and most compressive simulation skill of Rt and CREs over these three sub-regions in this study. This simulation difficulty demonstrates the complex and various cloud-radiation climatic processes in Asian monsoon regions. This study shows that the simulated Ts cold bias in CMIP6 models over the central and western TP is conducive to weaker OLR and larger surface albedo, causing larger upward shortwave radiation and weaker ASR (SWCRE). Meanwhile, considerable differences in cloud fractions, CREs, and their model performances also exist between the western and eastern TP. Further model assessment is therefore needed to well understand the simulation differences in cloud-radiation performances over the western and eastern TP. The underestimated intensity of Rt and NCRE over EC is highly correlated to underestimated low-middle cloud fractions associated with weaker regional ascending motion in current CMIP6 AMIP models. Besides, this underestimated cloud radiative cooling effect is also very likely related to large uncertainties in aerosol-cloud-radiation effects over EC where heavy aerosol loading is distributed (Gettelman and Sherwood, 2016; Li et al., 2016; Wu et al. 2016). Over SA, the underestimated HCF and OLR are related to weaker deep convection, which is probably caused by inappropriate convective parameterizations in present climate models. These biases and difficulties of cloud-radiation simulation should be further examined over the TP and adjacent monsoon regions with complex topography using more reliable reanalyzed meteorological and satellite-retrieved data.

Acknowledge

This work was supported by the National Science Foundation of China (91737306, 91837204, 41975109, and 41730963). CERES products used in this study were produced by the NASA CERES Team, available at http://ceres.larc.nasa.gov.

References

Adler, R. F., Huffman, G. J., Chang, A., Ferraro, R., Xie, P., Janowiak, J., Rudolf, B., Schneider, U., Curtis, S., Bolvin, D., Gruber, A., Susskind, J., & Arkin, P. (2003). The Version 2 Global Precipitation Climatology Project (GPCP) Monthly Precipitation Analysis (1979-Present). *Journal of Hydrometeorology*, 4, 1147–1167.

Allan, R. P., 2011: Combining satellite data and models to estimate cloud radiative effect at the surface and in the atmosphere. Meteorological Applications, 18, 324–333.

Bao, S. H., and Coauthors, (2019). Spatiotemporal distributions of cloud parameters and their response to meteorological factors over the Tibetan Plateau during 2003-2015 based on MODIS data. *International Journal of Climatology*, 39, 532-543.

Boo, K. O., Martin, G., Sellar, A., Senior, C., & Byun, Y. H. (2011). Evaluating the East Asian monsoon simulation in climate models. *Journal of Geophysical Research: Atmospheres*, 116(D1), D01109, doi:10.1029/2010JD014737.

Boucher, O., Randall, D., Artaxo, P., Bretherton, C., Feingold, G., Forster, P., Kerminen, V.-M., Kondo, Y., Liao, H., Lohmann, U., Rasch, P., Satheesh, S.K., Sherwood, S., Stevens, B. and Zhang, X.Y. (2013) Clouds and aerosols. In: Stocker, T.F., Qin, D., Plattner, G.-K., Tignor, M., Allen, S.K., Boschung, J., Nauels, A., Xia, Y., Bex, V. and Midgley, P.M. (Eds.) Climate Change 2013: The Physical Science Basis. Contribution of Working Group I to the Fifth Assessment Report of the Intergovernmental Panel on Climate Change. Cambridge, UK and New York, NY: Cambridge University Press.

Chen, G., and Wang, W. ‐ C. (2016). An effective approach to evaluate GCM simulated diurnal variation of clouds. *Geophysical Research Letters*, 43, 11,064–11,071, doi:10.1002/2016GL070446.

Chen, X. L., Liu, Y. M., & Wu, G. X. (2017). Understanding the Surface Temperature Cold Bias inCMIP5 AGCMs over the Tibetan Plateau. *Advances in Atmospheric Sciences*, 34(12), 1447–1460, doi:10.1007s00376-017-6326-9.

Chen, L., and O. W. Frauenfeld (2014). Surface air temperature changes over the twentieth and twenty-first centuries in china simulated by 20 CMIP5 models. *Journal of Climate*, 27(11), 3920–3937, doi: 10.1175/JCLI-D-13-00465.1.

Chepfer, H., Bony, S., Winker, D., Cesana, G., Dufresne, J. L., Minnis, P., Stubenrauch, C. J., & Zeng, S. (2010). The GCM-Oriented CALIPSO Cloud Product (CALIPSO-GOCCP). *Journal of Geophysical Research: Atmospheres*, 115, doi:10.1029/2009jd012251.

Dee, D. P., Uppala, S. M., Simmons, A. J. et al. (2011). The ERA-Interim reanalysis: Configuration and performance of the data assimilation system. *Quarterly Journal of the Royal Meteorological Society*, 137, 553–597.

Ding, Y., & Chan J. C. (2005). The East Asian summer monsoon: An overview, *Meteorology and Atmospheric Physics*, 89(1–4), 117–142.

Dolinar, E. K., X. Dong, B. Xi, J. H. Jiang, and H. Su, 2014: Evaluation of CMIP5 simulated clouds and TOA radiation budgets using NASA satellite observations. *Climate Dynamics*, 44, 2229–2247.

Duan, A. M., & Wu, G. X. (2009). Weakening Trend in the Atmospheric Heat Source over the Tibetan Plateau during Recent Decades. Part II: Connection with climate

warming. *Journal of Climate*, 22(15), 4197–4212.
Eyring, V., Bony, S., Meehl, G. A., Senior, C. A., Stevens, B., Stouffer, R. J. & Taylor, K. E. (2016). Overview of the Coupled Model Intercomparison Project Phase 6 (CMIP6) experimental design and organization. *Geoscientific Model Development*, 9, 1937–1958.
Flato, G., J. Marotzke, B. Abiodun, P. Braconnot, S.C. Chou, W. Collins, P. Cox, F. Driouech, S. Emori, V. Eyring, C. Forest, P. Gleckler, E. Guilyardi, C. Jakob, V. Kattsov, C. Reason and M. Rummukainen, 2013: Evaluation of Climate Models. In: Climate Change 2013: The Physical Science Basis. Contribution of Working Group I to the Fifth Assessment Report of the Intergovernmental Panel on Climate Change [Stocker, T.F., D. Qin, G.-K. Plattner, M. Tignor, S.K. Allen, J. Boschung, A. Nauels, Y. Xia, V. Bex and P.M. Midgley (eds.)]. Cambridge University Press, Cambridge, United Kingdom and New York, NY, USA.
Flohn, H. (1957). Large-scale aspects of the "summer monsoon" in South and East Asia. *Journal of the Meteorological Society of Japan*, 35, 180–186.
Fu. Y. F., Ma, Y. M., Zhong, L., Yang, Y. J., Guo, X. L., Wang, C. H., Xu, X. F., Yang, K., Xu, X. D., Liu, L. P., Fan, G. Z., Li, Y. Q., & Wang, D. H. (2020). Land-surface processes and summer-cloud-precipitation characteristics in the Tibetan Plateau and their effects on downstream weather: a review and perspective. *National Science Review*, 7(3), 500–515.
Gettelman, A., & Sherwood, S. C. (2016). Processes Responsible for Cloud Feedback, *Current Climate Change Reports*, 2(4), 179–189.
Haarsma, R. J., Roberts, M. J., Vidale, P. L., Senior, C. A., Bellucci, A., Bao, Q., et al. (2016). High Resolution Model Intercomparison Project (HighResMIP v1.0) for CMIP6, *Geoscientific Model Development*, 9, 4185–4208.
Hartmann, D. L., Moy, L. A. & Fu, Q. (2001). Tropical Convection and the Energy Balance at the Top of the Atmosphere. *Journal of Climate*, 14, 4495–4511.
He, J. H., P. Zhao, C. W. Zhu, R. H. Zhang, and X. Tang, 2008: Discussions on the East Asian subtropical monsoon. *Acta Meteorologica Sinica*, 66(5), 683–696.
Huang, D.-Q., Zhu, J., Zhang, Y. C., Huang, Y., & Kuang, X. Y. (2016). Assessment of summer monsoon precipitation derived from five reanalysis datasets over East Asia, *Quarterly Journal of the Royal Meteorological Society*, 142(694), 108–119, doi:10.1002/qj.2634.
Kiehl, J. T., 1994: On the Observed Near Cancellation between Longwave and Shortwave Cloud Forcing in Tropical Regions. *Journal of Climate*, 7, 559–565.
Lauer, A. & Hamilton, K. (2013). Simulating Clouds with Global Climate Models: A Comparison of CMIP5 Results with CMIP3 and Satellite Data. *Journal of Climate*, 26, 3823–3845.
Li, J. D., You, Q. L. & He, B. (2020). Distinctive spring shortwave cloud radiative effect and its interannual variation over southeastern China. *Atmospheric Science Letters*, 21:e970, doi: 10.1002/asl.970.
Li, J. D., Wang, W. C., Mao, J. Y., Wang, Z. Q., Zeng G., & Chen, G. X. (2019). Persistent spring cloud shortwave radiative effect and the associated circulations over southeastern China. *Journal of Climate*, 32, 3069–3087.

Li, J. D., Wang, W. C., Dong, X. Q., & Mao, J. Y. (2017). Cloud-radiation-precipitation associations over the Asian monsoon region: an observational analysis. *Climate Dynamics*, 49(9), 3237–3255.

Li, J. L., Waliser, D., Stephens, G., Lee, S., L'Ecuyer, T., Kato, S., Loeb, N., & Ma H. Y. (2013). Characterizing and understanding radiation budget biases in CMIP3/CMIP5 GCMs, contemporary GCM, and reanalysis. *Journal of Geophysical Research: Atmospheres*, 118, 8166–8184, doi:10.1002/jgrd.50378.

Li, Y., Liu, X., & Chen, B. (2006). Cloud type climatology over the Tibetan Plateau: a comparison of ISCCP and MODIS/TERRA easurements with surface observations. *Geophysical Research Letters*, 33, 130–142.

Li, Z. Q., et al. (2016). Aerosol and monsoon climate interactions over Asia. *Reviews of Geophysics*, *54*(4), 866–929.

Liang, X. Z. & Wang, W. C. (1998). Associations between China monsoon rainfall and tropospheric jets. *Quarterly Journal of the Royal Meteorological Society*, 124(552), 2597–2623.

Liu, Y. M., Lu, M. M., Yang, H. J., Duan, A. M., He, B., Yang, S., & Wu, G. X. (2020). Land–atmosphere–ocean coupling associated with the Tibetan Plateau and its climate impacts. *National Science Review*, 7(3), 534–552.

Loeb, N. G., and Coauthors, 2018: Clouds and the Earth's Radiant Energy System (CERES) Energy Balanced and Filled (EBAF) Top-of-Atmosphere (TOA) Edition-4.0 Data Product. *Journal of Climate,* 31, 895-918.

Luo, Y. L., Zhang, R. H., Qian, W. M., et al. 2011. Intercomparison of deep convection over the Tibetan Plateau–Asian monsoon region and subtropical North America in boreal summer using CloudSat/CALIPSO data. *Journal of Climate*, 24 (8): 2164–2177, doi:10.1175/2010JCLI4032.1.

Ma, Q. R., You, Q. L., Ma, Y. J., Cao, Y., & Zhang, J. (2021). Changes in cloud amount over the Tibetan Plateau and impacts of large-scale circulation. *Atmospheric Research*, 249, 105332, doi:10.1016/j.atmosres.2020.105332

Myhre, G., D. Shindell, F.-M. Bréon, W. Collins, J. Fuglestvedt, J. Huang, D. Koch, J.-F. Lamarque, D. Lee, B. Mendoza, T. Nakajima, A. Robock, G. Stephens, T. Takemura and H. Zhang, 2013: Anthropogenic and Natural Radiative Forcing. In: Climate Change 2013: The Physical Science Basis. Contribution of Working Group I to the Fifth Assessment Report of the Intergovernmental Panel on Climate Change [Stocker, T.F., D. Qin, G.-K. Plattner, M. Tignor, S.K. Allen, J. Boschung, A. Nauels, Y. Xia, V. Bex and P.M. Midgley (eds.)]. Cambridge University Press, Cambridge, United Kingdom and New York, NY, USA.

Pan, Z., W. Gong, F. Mao, J. Li, W. Wang, C. Li, and Q. Min, 2015: Macrophysical and optical properties of clouds over East Asia measured by CALIPSO. *Journal of Geophysical Research: Atmospheres*, 120, 11,653–611,668.

Rajeevan, M., and Srinivasan, J. (2000). Net cloud radiative forcing at the top of the atmosphere in the Asian monsoon region. *Journal of Climate,* 13(3), 650–657.

Ramanathan, V., 1987: The role of earth radiative budget studies in climate and general circulation research. *Journal of Geophysical Research: Atmospheres*, 92(D4), 4075–4095.

Pincus, R., Batstone, C. P., Hofmann, R. J. P., Taylor, K. E., & Glecker, P. J. (2008). Evaluating the present-day simulation of clouds, precipitation, and radiation in climate models. *Journal of Geophysical Research: Atmospheres*, 113(D14), doi:10.1029/2007jd009334.

Sperber, K., and Coauthors, 2013: The Asian summer monsoon: an intercomparison of CMIP5 vs. CMIP3 simulations of the late 20th century. *Climate Dynamics*, 41, 2711–2744.

Saud, T., Dey, S., Das, S., & Dutta, S. (2016). A satellite-based 13-year climatology of net cloud radiative forcing over the Indian monsoon region. *Atmospheric Research*, 182, 76–86.

Shindell, D. T., Lamarque, J. F., Schulz, M., Flanner, M. and others (2013). Radiative forcing in the ACCMIP historical and future climate simulations. *Atmospheric Chemistry Physics*, 13: 2939–2974

Stephens, G.L. (2005) Cloud feedbacks in the climate system: a critical review. *Journal of Climate*, 18, 237–273.

Tao, S. Y., & Chen., L. X. (1987). A review of recent research on the East Asian summer monsoon in China. *Monsoon Meteorology*, 60–92.

Taylor, K. E. (2001). Summarizing multiple aspects of model performance in a single diagram. *Journal of Geophysical Research: Atmospheres*, 106(D7), 7183–7192, doi:10.1029/2000jd900719.

Taylor, K. E., Stouffer, R. J., & Meehl, G. A. (2012). An Overview of CMIP5 and the Experiment Design. *Bulletin of the American Meteorological Society*, 93, 485-498.

Trenberth, K. E., Fasullo, J. T., & Kiehl, J. (2009). Earth's global energy budget. *Bulletin of the American Meteorological Society*, 90(3), 311–323.

Turner, A. G., & Annamalai, H. (2012). Climate change and the South Asian summer monsoon. *Nature Climate Change*, 2, 587–595.

Wang, A., & Zeng, X. (2012). Evaluation of multi-reanalysis products with in situ observations over the Tibetan Plateau. *Journal of Geophysical Research: Atmosphere*, doi:10.1029/2011JD016553.

Wang, B., Biasutti, M., Byrne, M. P, Castro, C., Chang, C-P., Cook, K., et al. (2020). Monsoons climate change assessment. *Bulletin of the American Meteorological Society*, https://doi.org/10.1175/BAMS-D-19-0335.1.

Wang, F., Yang, S., & Wu, T. W. (2014). Radiation budget biases in AMIP5 models over the East Asian monsoon region. *Journal of Geophysical Research: Atmosphere*, 119(23), 13400-13426, doi:10.1002/2014JD022243.

Wang, H., Luo, Y. L., & Zhang, R. H. (2011) Analyzing seasonal variation of clouds over the Asian monsoon regions and the Tibetan Plateau Region using CloudSat/CALIPSO data. *Chinese Journal of Atmospheric Sciences (in Chinese)*, 35 (6): 1117–1131.

Wang, W. C., Gong, W., Kau, W. S., Chen, C. T., Hsu, H. H., & Tu, C. H. (2004). Characteristics of cloud radiation forcing over east China. *Journal of Climate*, 17, 845–853.

Wang, Z. Q., Duan, A. M., & Wu, G. X. (2014). Time-lagged impact of spring sensible heat over the Tibetan Plateau on the summer rainfall anomaly in East China: Case

studies using the WRF model. *Climate Dynamics*, 42(11-12), 2885–2898.
Webb, M. J., et al. (2017), The Cloud Feedback Model Intercomparison Project (CFMIP) contribution to CMIP6. *Geoscientific Model Development*, 10(1), 359–384.
Webster, P. J., V. O. Magaña, T. N. Palmer, J. Shukla, R. A. Tomas, M. Yanai, and T. Yasunari, 1998: Monsoons: Processes, predictability, and the prospects for prediction. *Journal of Geophysical Research: Oceans*, 103, 14451–14510.
Wu, G. X., Li, Z. Q., Fu, C. B., Zhang, X. Y., Zhang, R. Y., Zhang, R. H., Zhou, T. J., Li, J. P., Li, J. D., Zhou, D. G., Wu, L., Zhou, L. T., He, B. & Huang, R. H. (2016). Advances in studying interactions between aerosols and monsoon in China. *Science China: Earth Sciences*, 59, 1–16.
Wu, G. X., Duan, A. M., Liu, Y. M., Mao, J. Y., Ren, R. C., Bao, Q., He, B., Liu, B. Q. & W. T. Hu (2015). Tibetan Plateau climate dynamics: recent research progress and outlook. *National Science Review*, 2(1), 100–116.
Wu, G. X., Liu, Y. M., Wang, T. M., Wan, R. J., Liu, X., Li, W. P., Wang, Z. Z., Zhang, Q., Duan, A. M., & Liang, X. Y. (2007). The influence of mechanical and thermal forcing by the Tibetan Plateau on Asian climate. *Journal of Hydrometeorology*, 8(4), 770–789.
Xu, X. D., Zhao, T. L., Shi, X. H., & Lu, C.G. (2015). A study of the role of the Tibetan Plateau's thermal forcing in modulating rainband and moisture transport in eastern China. *Acta Meteorologica Sinica*, 73, 20–35.
Yan, Y. F., Liu, Y. M., & Lu, J. H. (2016). Cloud vertical structure, precipitation, and cloud radiative effects over Tibetan Plateau and its neighboring regions. *Journal of Geophysical Research: Atmosphere*, 121(10), 5864–5877, doi:10.1002/2015JD024591.
Yanai, M., Li, C., Song, Z., 1992. Seasonal heating of the Tibetan Plateau and its effects on the evolution of the Asian summer monsoon. *Journal of the Meteorological Society of Japan*, 70, 319–351.
Yang, K., H. Wu J. Qin, C. Lin, W. Tang, & Y. Chen, 2014: Recent climate changes over the Tibetan Plateau and their impacts on energy and water cycle: A review. *Global and Planetary Change*, 112, 79–91.
Yeh, T. C, Luo, S. W., & Chu, P. C. (1957). The wind structure and heat balance in the lower troposphere over Tibetan Plateau and its surrounding. *Acta Meteorologica Sinica*, 28, 108–121.
You, Q., Chen, D., Wu, F., Pepin, N., Cai, Z., Ahrens, B., Jiang, Z., Wu, Z., Kang, S., & AghaKouchak, A., (2020). Elevation dependent warming over the Tibetan Plateau: Patterns, mechanisms and perspectives. *Earth-Science Reviews*, 210, 103349, doi:10.1016/j.earscirev.2020.103349.
You, Q., A. Sanchez-Lorenzo, M. Wild, D. Folini, K. Fraedrich, G. Ren, & S. Kang (2012), Decadal variation of surface solar radiation in the Tibetan Plateau from observations, reanalysis and model simulations. *Climate Dynamics*, 40(7-8), 2073–2086, doi:10.1007/s00382-012-1383-3.
Yu, R. C., Yu, Y. Q., & Zhang, M. H. (2001). Comparing cloud radiative properties between the eastern China and the Indian monsoon region. *Advances in Atmospheric Sciences*, 18, 1090–1102.

Yu, R. C., Wang, B., & Zhou, T. J. (2004). Climate effects of the deep continental stratus clouds generated by the Tibetan Plateau. *Journal of Climate*, 17, 2702–2713.

Zhang, B. C., Guo, Z., Zhang, L. X., Zhou, T. J., & Hayasaya, T. (2020). Cloud Characteristics and Radiation Forcing in the Global Land Monsoon Region From Multisource Satellite Data Sets. *Earth and Space Science*, 7(3), doi:10.1029/2019EA001027.

Zhang H., & Jing, X. W. (2016). Advances in studies of cloud overlap and its radiative transfer in climate models. *Journal of Meteorological Research*, 30(2), 156–168.

Zhang, Y., Chen, H., & Yu, R. (2015). Simulations of Stratus Clouds over Eastern China in CAM5: Sources of Errors. *Journal of Climate*, 28, 36–55.

Zhang, Y., & Li, J. (2013). Shortwave cloud radiative forcing on major stratus cloud regions in AMIP-type simulations of CMIP3 and CMIP5 models. *Advances in Atmospheric Sciences*, 30(3), 884–907.

Zhao, C., Y. Chen, J. Li, H. Letu, Y. Su, T. Chen, and X. Wu, 2019: Fifteen-year statistical analysis of cloud characteristics over China using Terra and Aqua Moderate Resolution Imaging Spectroradiometer observations. *International Journal of Climatology*, 39, 2612–2629.

Zhou, T., and Coauthors, 2016: GMMIP (v1.0) contribution to CMIP6: Global Monsoons Model Inter-comparison Project. *Geoscientific Model Development*, 9, 3589–3604.

Zhou., X. J., Zhao, P., Chen, J. M., Chen, L. X., & Li, W. L. (2009). Impacts of thermodynamic processes over the Tibetan Plateau on the Northern Hemispheric climate. *Science in China Series D: Earth Sciences*, 52(11): 1679–1693.

Zhou, Y., Y. Zhang, X. Rong, J. Li, and R. Yu, 2019: Performance of CAMS-CSM in Simulating the Shortwave Cloud Radiative Effect over Global Stratus Cloud Regions: Baseline Evaluation and Sensitivity Test. *Journal of Meteorological Research*, 33, 651–665.

Tables

Table 1. CMIP6 AMIP models used in this study. The model with an arterisk has the satellite simulator output.

Table 2. Abbreviations of variable names used in this study.

Table 3. Annual mean top-of-atmosphere (TOA) radiation fluxes and cloud radiative effects (CREs) from CERES-EBAF averaged over Eastern China (EC: 22-32° N, 102-122° E), South Asia (SA: 15.5-25.5° N, 80-100° E) and the Tibetan Plateau (TP: 27.5-37.5° N, 80-100° E). Units: W m^{-2}.

Table 4. The regional mean TOA radiation fluxes and CREs (W m^{-2}) from Multi-model mean (MME), their overall bias (W m^{-2}) and relative bias (RB) relative to observations, and spatial pattern correlation coefficient (PCC) between MME and the observation over EC, SA and the TP.

Table 5. The standard deviation (STD) of monthly Rt and NCRE from the observation and CMIP6 MME, respectively, and the temporal correlation coefficients between MME and the observation averaged over EC, SA and the TP during 2001-2014.

Figures

Figure 1. Distribution of annual mean (a-b) top-of-atmosphere (TOA) Radiation budget (Rt; unit: W m^{-2}) and net cloud radiative effect (NCRE; unit: W m^{-2}) from CERES-EBAF, and (c) topography (m). In (c), three black boxes denote Eastern China (EC: 22-32° N, 102-122° E), South Asia (SA: 15.5-25.5° N, 80-100° E) and the Tibetan Plateau (TP: 27.5-37.5° N, 80-100° E), respectively.

Figure 2. Distribution of (a-g) TOA incident solar radiation (ASR; unit: W m^{-2}), outgoing longwave radiation (OLR; unit: W m^{-2}), surface albedo, shortwave cloud radiative effect (SWCRE; unit: W m^{-2}), longwave cloud radiative effect (LWCRE; unit: W m^{-2}) from CERES-EBAF during 2001-2014 and total cloud fraction (TCF; unit: %) from GOCCP during 2007-2014.

Figure 3. Distribution of annual mean Rt (W m^{-2}) simulated by (a-bb) CMIP6 AMIP models and MME, and (cc) in the observation during 2001-2014.

Figure 4. Annual mean (a, b, c) TOA Rt, ASR (W m^{-2}) and OLR (W m^{-2}) simulated by CMIP6 AMIP models and MME, and in the observation averaged over EC (Figures 5a, d, g), SA (Figures 5b, e, h) and the TP (Figures 5c, f, i). Here, red and blue lines denote the observation and MME, respectively.

Figure 5. Pattern correlation coefficient and standard center RMSE between annual mean CMIP6 AMIP model and observational counterparts for TOA Rt, ASR and OLR over EC (Figures 6a, b, c), SA (Figures 6d, e, f) and the TP (Figures 6g, h, i). The center RMSE from a specific model is divided by the STD of observational counterpart.

Figure 6. Distribution of annual mean NCRE (W m^{-2}) simulated by (a-bb) CMIP6 AMIP models and MME, and (cc) in the observation during 2001-2014.

Figure 7. Annual mean (a, b, c) NCRE, SWCRE and LWCRE simulated by CMIP6 AMIP models and MME (unit: W m^{-2}), and in the observation averaged over EC (Figures 7a, d, g), SA (Figures 7b, e, h) and the TP (Figures 7c, f, i). Here, red and blue lines denote the observation and MME, respectively.

Figure 8. Pattern correlation coefficient and standard center RMSE between annual mean CMIP6 AMIP model and observational counterparts for NCRE, SWCRE and LWCRE over EC (Figures 8a, b, c), SA (Figures 8d, e, f) and the TP (Figures 8g, h, i).

Figure 9. Seasonal cycles of simulated monthly and regional mean (a, d, and g) Rt, (b, e, and h) ASR, and (c, f, and i) OLR (unit: W m^{-2}) averaged over EC (Figures 9a–9c), SA (Figures 9d–9f), and the TP (Figures 9g–9i). The red and black solid lines denote the observation and MME, respectively. The black box indicates the standard deviation among the models. Here, the period is 2001-2014. The number at x axis is the month number.

Figure 10. Pattern correlation coefficient and standard RMSE between annual cycles of CMIP6 AMIP model and observational counterparts for TOA Rt, ASR and OLR over EC (Figures 11a-11c), SA (Figures 11d-11f) and the TP (Figures 11g-11i) during 2001-2014. The center RMSE from a specific model is divided by the STD of observational counterpart.

Figure 11. Seasonal cycles of simulated monthly and regional mean (a, d, and g) NCRE, (b, e, and h) SWCRE, and (c, f, and i) LWCRE (unit: W m^{-2}) averaged over EC (Figures 10a–10c), SA (Figures 10d–10f), and the TP (Figures 10g–10i). The red and black solid lines denote the observation and MME, respectively. The black box indicates the standard deviation among the models. The number at x axis is the month number.

Figure 12. Pattern correlation coefficient and standard RMSE between annual cycles

of CMIP6 AMIP model and observational counterparts for NCRE, SWCRE and LWCRE over EC (Figures 12a-12c), SA (Figures 12d-12f) and the TP (Figures 12g-12i) during 2001-2014. The center RMSE from a specific model is divided by the STD of observational counterpart.

Figure 13. Distribution of annual mean biases of (a-i) Rt, ASR, OLR, RSUT, RSUTCS, OLRC, NCRE, SWCRE and LWCRE (unit: W m^{-2}) during 2001-2014 simulated from CMIP6 AMIP MME.

Figure 14. Seasonal cycles of monthly and regional mean (a, b, and c) TCF and (d, e, and f) HCF (unit: %) averaged over EC (Figures 14a, 14d), SA (Figures 14b, 14e), and the TP (Figures 14c, 14f) simulated by 9 CMIP6 models with satellite simulator output during 2007-2014. The red and black solid lines denote the observation and MME, respectively. The black box indicates the standard deviation among the models. The number at x axis is the month number.

Figure 15. Distribution of (a-c) NCRE, SWCRE and LWCRE (W m^{-2}) in CMIP6 AMIP MME with satellite simulator output, and differences in (a-f) TCF, LCF, HCF (%), NCRE, SWCRE and LWCRE (W m^{-2}) between CMIP6 AMIP MME with satellite simulator output and GOCCP during 2007-2014.

Figure 16. Distribution of (a-b) observational circulation condition and surface temperature (K), and (c-d) their differences between CMIP6 AMIP MME with satellite simulator output and the counterparts from ERA-Interim reanalysis during 2007-2014. In (a) and (c), black contours represent 200-hPa zonal wind speed (m s^{-1}) or its simulated biases relative to ERA-Interim analysis; arrows represent the 850-hPa wind field, with the graphic at top right showing an arrow corresponding to 5 (2) m s^{-1}; the black counter represents the TP topography (>3000m).

Table 1. CMIP6 AMIP models used in this study. The model with an arterisk has the satellite simulator output.

Model ID	Model name	Spatial resolution (Lat×Lon: degree)
1	ACCESS-CM2	1.25×1.875
2	ACCESS-ESM1-5	1.25×1.875
3	BCC-CSM2-MR	1.12×1.125
4	BCC-ESM1	2.79×2.8125
5	CanESM5	2.79×2.8125
6	CAMS-CSM1-0	1.12×1.125
7	CESM2*	0.9424×1.25
8	CNRM-CM6-1	1.40×1.40625
9	CNRM-CM6-1-HR	0.50×0.50
10	CNRM-ESM2-1*	1.40×1.40625
11	E3SM-1-0*	1.0×1.0
12	FGOALS-f3-L	1.0×1.25
13	FGOALS-g3	2.0×2.025
14	GFDL-AM4	1.0×1.25
15	GISS-E2-1	1.0×2.5
16	HadGEM3-GC31-LL	1.25×1.875
17	HadGEM3-GC31-MM*	0.56×0.83
18	INM-CM5-0	2.0×1.5
19	IPSL-CM6A-LR*	1.2676×2.5
20	KACE-1-0-G	1.25×1.875
21	MIROC6*	1.4007×1.40625
22	MRI-ESM2-0*	1.1214×1.125
23	MPI-ESM1-2-HR	0.935×0.9375
24	NESM3	1.865×1.875
25	NorESM2-LM*	1.8947×2.5
26	SAM0-UNICON	0.9424×1.25
27	UKESM1-0-LL*	1.25×1.875

Table 2. Abbreviations of variable names used in this study.

Variable name	Physical meaning	Unit	Sign
TOA	Top of atmosphere	None	None
LWCRE	Longwave cloud radiation effect	W m^{-2}	+
SWCRE	Shortwave cloud radiation effect	W m^{-2}	−
NCRE	Net cloud radiation effect	W m^{-2}	Generally, minus
ASR	TOA net incident shortwave radiation	W m^{-2}	+
OLR	Outgoing longwave radiation flux at the TOA under all-sky condition	W m^{-2}	+
OLRCS	Outgoing longwave radiation flux at the TOA under clear-sky condition	W m^{-2}	+
RSDT	Incident solar radiation at the TOA	W m^{-2}	+
RSUT	Outgoing shortwave radiation fluxe at the TOA under all-sky condition	W m^{-2}	+
RSUTCS	Outgoing shortwave radiation fluxe at the TOA under clear-sky condition	W m^{-2}	+
Rt	Radiation budget (equal to net radiation flux) at the TOA	W m^{-2}	Regional dependency
W_{500}	500-hPa vertical velocity	hPa d^{-1}	−
TCF	Total cloud fraction	%	+
HCF	High cloud fraction	%	+
MCF	Middle cloud fraction	%	+
LCF	Low cloud fraction	%	+
PCC	Pattern correlation coefficient	None	None
RB	Relative bias	None	None
RMSE	Root-mean-square-error	None	None
STD	Standard deviation	None	None
BOB	the Bay of Bagel	None	None
EC	Eastern China	None	None
SA	South Asia	None	None
TP	Tibetan Plateau	None	None
GPCP	Global Precipitation Climatology Project	None	None
AMIP	Atmospheric Model Intercomparison Project	None	None
MME	Multi-model mean	None	None

Table 3. Annual mean top-of-atmosphere (TOA) radiation fluxes and cloud radiative effects (CREs) from CERES-EBAF averaged over Eastern China (EC: 22-32° N, 102-122° E), South Asia (SA: 15.5-25.5° N, 80-100° E) and the Tibetan Plateau (TP: 27.5-37.5° N, 80-100° E). Units: W m^{-2}.

	EC	SA	TP
RSDT	374.1	391.1	356.4
ASR	231.8	281.9	228.0
RSUT	142.3	109.3	128.4
OLR	243.8	253.1	220.3
Rt	-12.0	28.8	7.7
LWCRE	34.8	37.8	28.3
SWCRE	-83.2	-50.1	-53.0
NCRE	-48.5	-12.3	-24.7

Table 4. The regional mean TOA radiation fluxes and CREs (W m^{-2}) from Multi-model mean (MME), their overall bias (W m^{-2}) and relative bias (RB) relative to observations, and spatial pattern correlation coefficient (PCC) between MME and the observation over EC, SA and the TP.

MME	Metrics	EC	SA	TP
Rt	Mean/Bias	1.0/13.0	26.0/-2.8	3.7/-4.0
	RB	-108.6%	-9.6%	-52.5%
	PCC	0.76	0.94	0.48
ASR	Mean/Bias	246.6/14.8	282.5/0.6	217.9/-10.2
	RB	6.4%	0.2%	-4.5%
	PCC	0.89	0.95	0.66
OLR	Mean/Bias	245.6/1.8	256.5/3.4	214.2/-6.1
	RB	0.7%	1.3%	-2.8%
	PCC	0.94	0.83	0.94
OLRC	Mean/Bias	269.8/-8.7	285.0/-5.9	238.5/-10.1
	RB	-3.1%	-2.0%	-4.1%
	PCC	0.97	0.96	0.92
RSUT	Mean/Bias	127.5/-14.8	108.8/-0.5	138.6/10.2
	RB	-10.4%	0.5%	8.0%
	PCC	0.83	0.89	0.50
RSUTC	Mean/Bias	53.2/7.2	61.6/2.4	96.8/21.4
	RB	12.2%	4.1%	28.3%
	PCC	0.86	0.95	0.68
NCRE	Mean/Bias	-37.0/11.5	-18.6/-6.4	-17.5/7.2
	RB	-23.8%	51.8%	-29.2%
	PCC	0.59	0.74	0.87
SWCRE	Mean/Bias	-61.2/22.0	-47.2/2.9	-41.8/11.2
	RB	-26.4%	-5.9%	-21.1%
	PCC	0.52	0.77	0.92
LWCRE	Mean/Bias	24.3/-10.5	28.5/-9.3	24.4/-4.0
	RB	-30.1%	-24.6%	-14.0%
	PCC	0.31	0.75	0.61

Table 5. The standard deviation (STD) of monthly Rt and NCRE from the observation and CMIP6 MME, respectively, and the temporal correlation coefficients between MME and the observation averaged over EC, SA and the TP during 2001-2014.

	Rt STD (W m^{-2})		NCRE STD (W m^{-2})		Correlation between Rt and NCRE	
	OBS	MME	OBS	MME	OBS	MME
EC	7.76	2.14	8.53	2.43	0.93	0.85
SA	4.19	2.19	3.72	1.58	0.73	0.67
TP	3.64	1.19	4.67	1.04	0.75	0.42

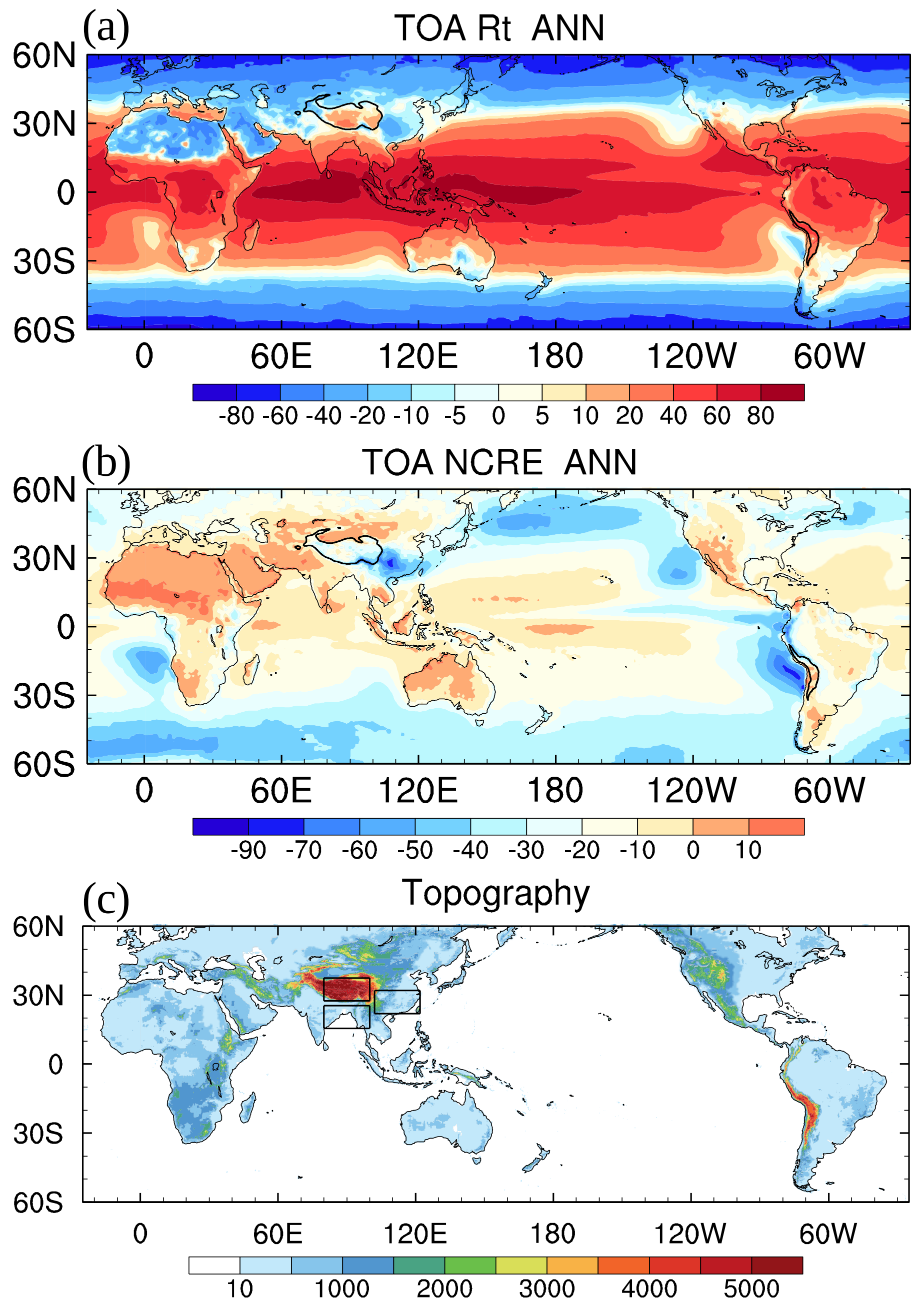

Figure 1. Distribution of annual mean (a-b) top-of-atmosphere (TOA) Radiation budget (Rt; unit: W m^{-2}) and net cloud radiative effect (NCRE; unit: W m^{-2}) from CERES-EBAF, and (c) topography (m). In (c), three black boxes denote Eastern China (EC: 22-32° N, 102-122° E), South Asia (SA: 15.5-25.5° N, 80-100° E) and the Tibetan Plateau (TP: 27.5-37.5° N, 80-100° E), respectively.

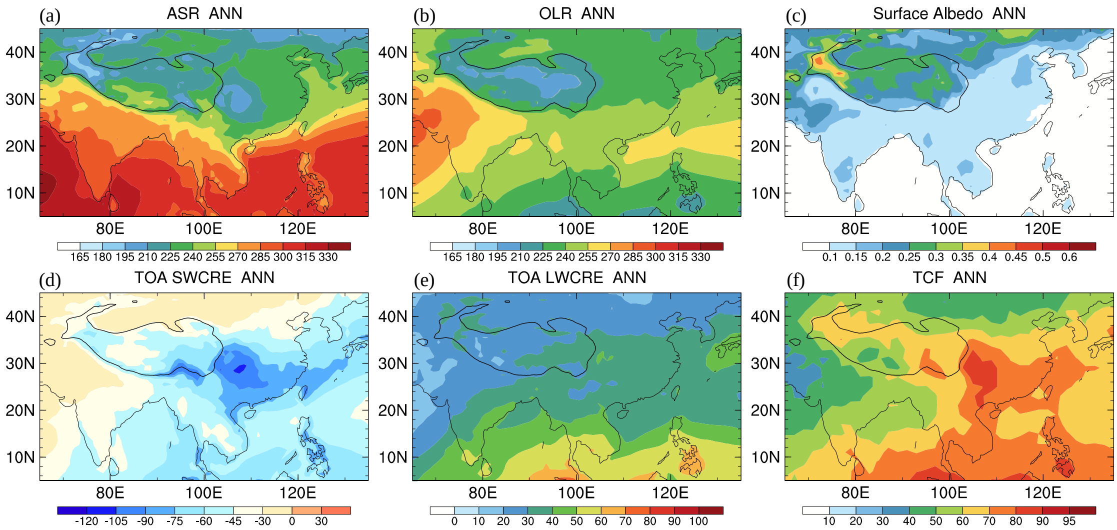

Figure 2. Distribution of (a-g) TOA incident solar radiation (ASR; unit: W m^{-2}), outgoing longwave radiation (OLR; unit: W m^{-2}), surface albedo, shortwave cloud radiative effect (SWCRE; unit: W m^{-2}), longwave cloud radiative effect (LWCRE; unit: W m^{-2}) from CERES-EBAF during 2001-2014 and total cloud fraction (TCF; unit: %) from GOCCP during 2007-2014.

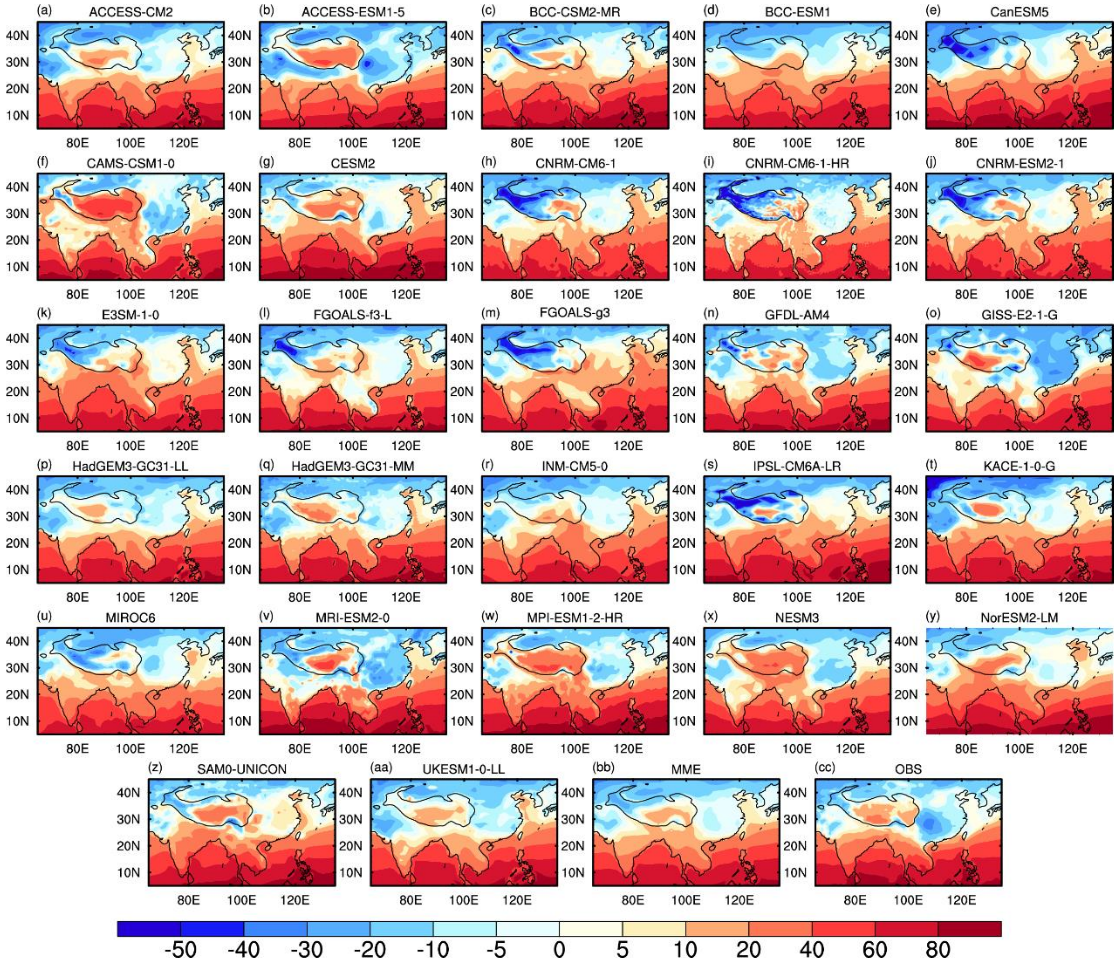

Figure 3. Distribution of annual mean Rt (W m^{-2}) simulated by (a-bb) CMIP6 AMIP models and MME, and (cc) in the observation during 2001-2014.

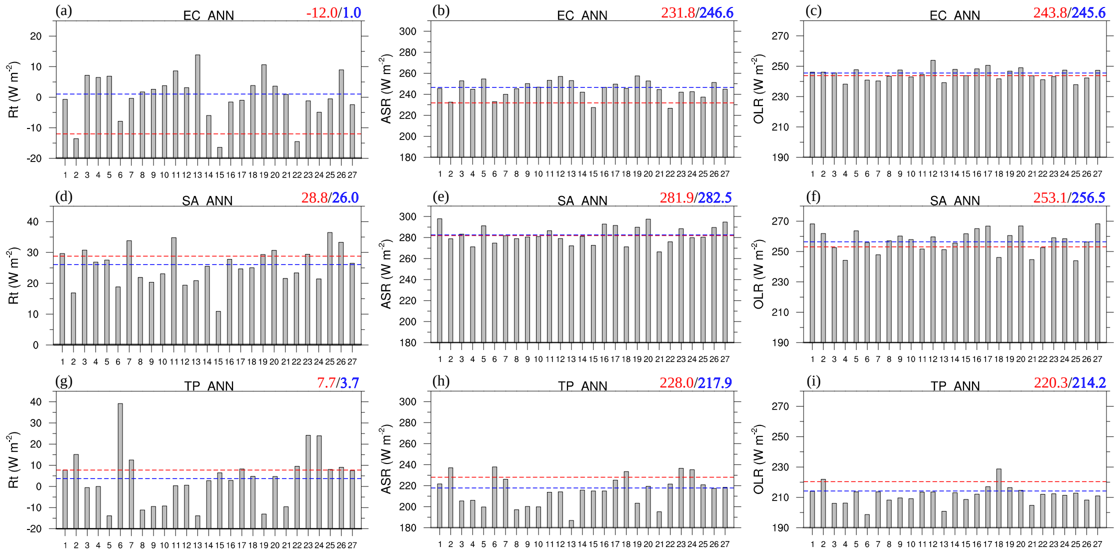

Figure 4. Annual mean (a, b, c) TOA Rt, ASR (W m^{-2}) and OLR (W m^{-2}) simulated by CMIP6 AMIP models and MME, and in the observation averaged over EC (Figures 5a, d, g), SA (Figures 5b, e, h) and the TP (Figures 5c, f, i). Here, red and blue lines denote the observation and MME, respectively.

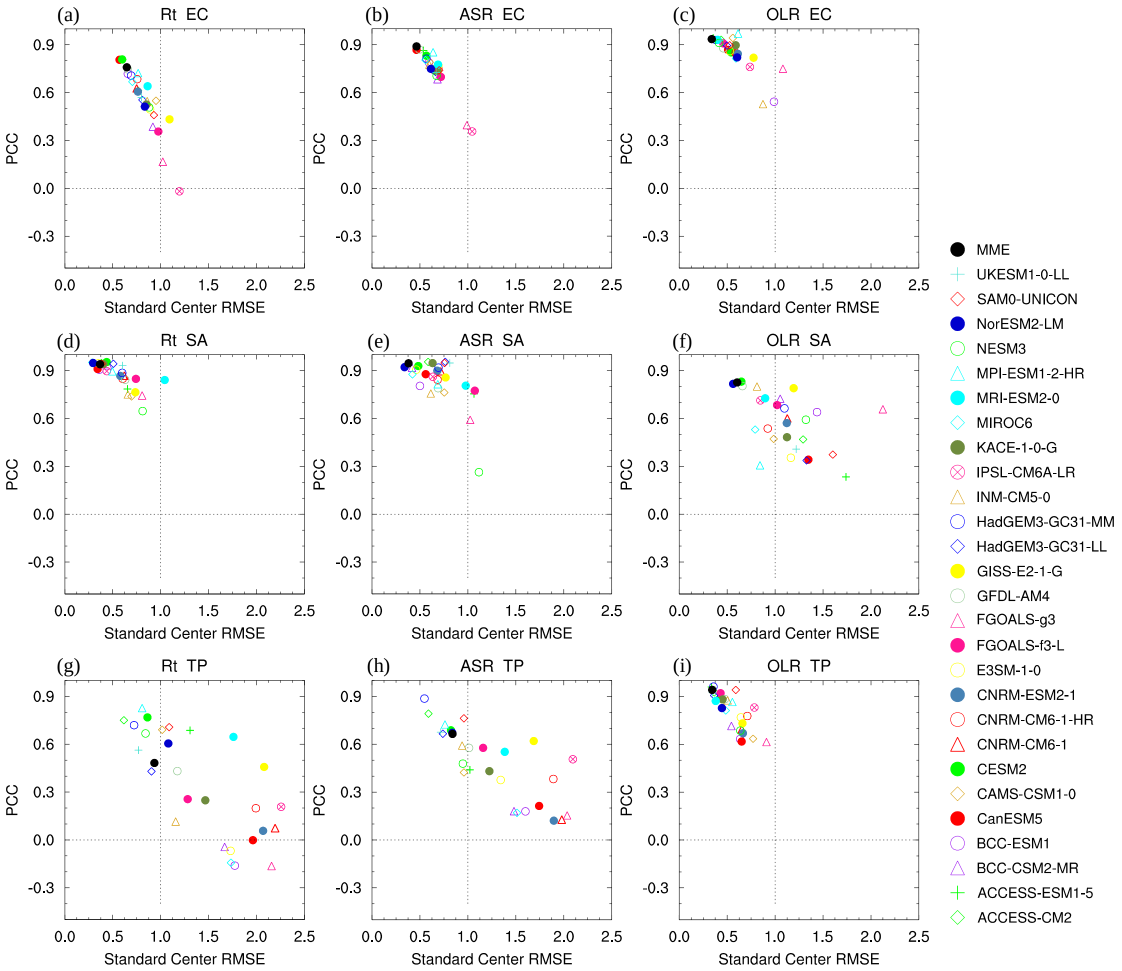

Figure 5. Pattern correlation coefficient and standard center RMSE between annual mean CMIP6 AMIP model and observational counterparts for TOA Rt, ASR and OLR over EC (Figures 6a, b, c), SA (Figures 6d, e, f) and the TP (Figures 6g, h, i). The center RMSE from a specific model is divided by the STD of observational counterpart.

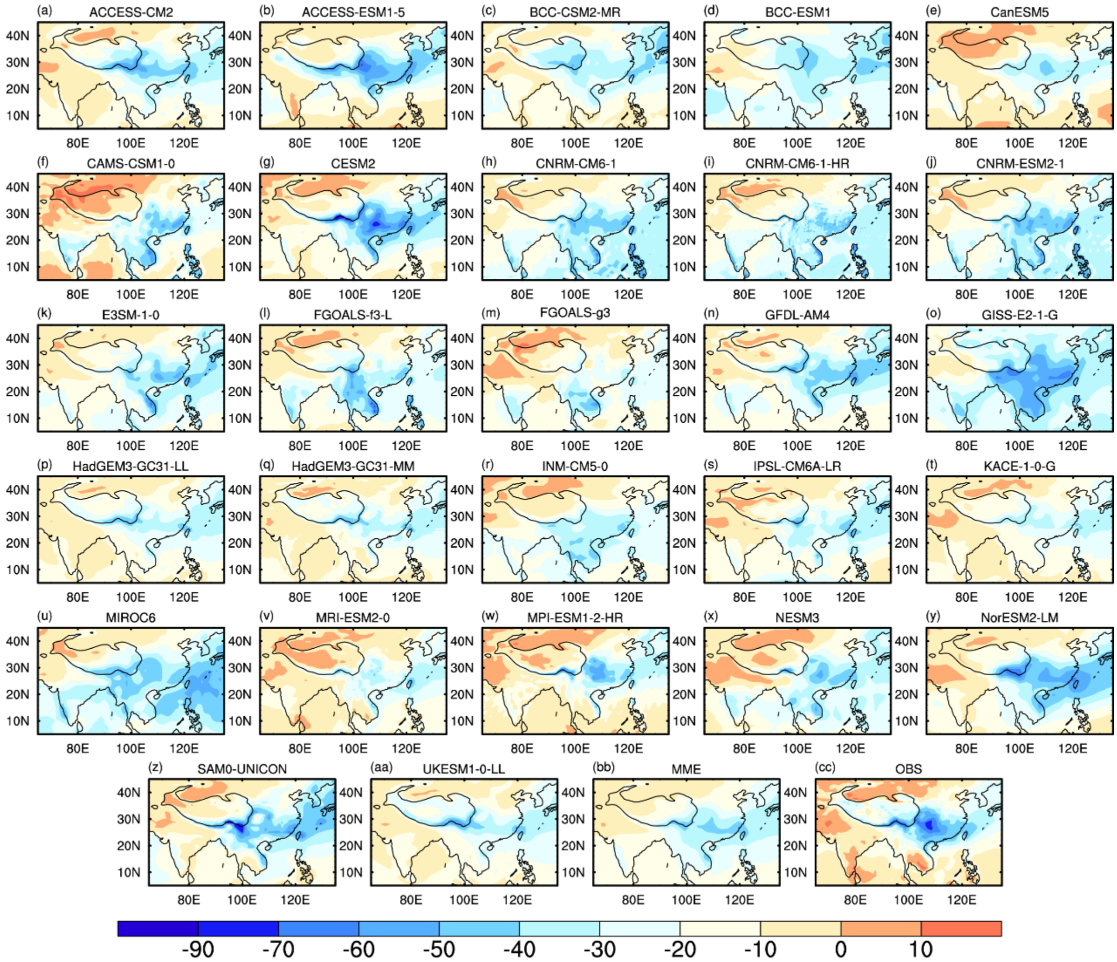

Figure 6. Distribution of annual mean NCRE (W m^{-2}) simulated by (a-bb) CMIP6 AMIP models and MME, and (cc) in the observation during 2001-2014.

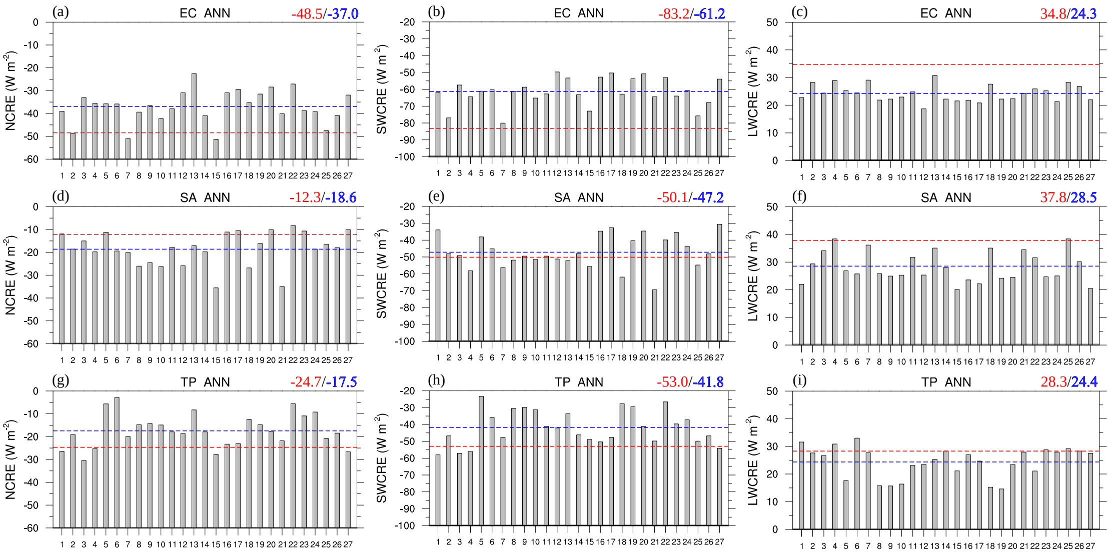

Figure 7. Annual mean (a, b, c) NCRE, SWCRE and LWCRE simulated by CMIP6 AMIP models and MME (unit: W m^{-2}), and in the observation averaged over EC (Figures 7a, d, g), SA (Figures 7b, e, h) and the TP (Figures 7c, f, i). Here, red and blue lines denote the observation and MME, respectively.

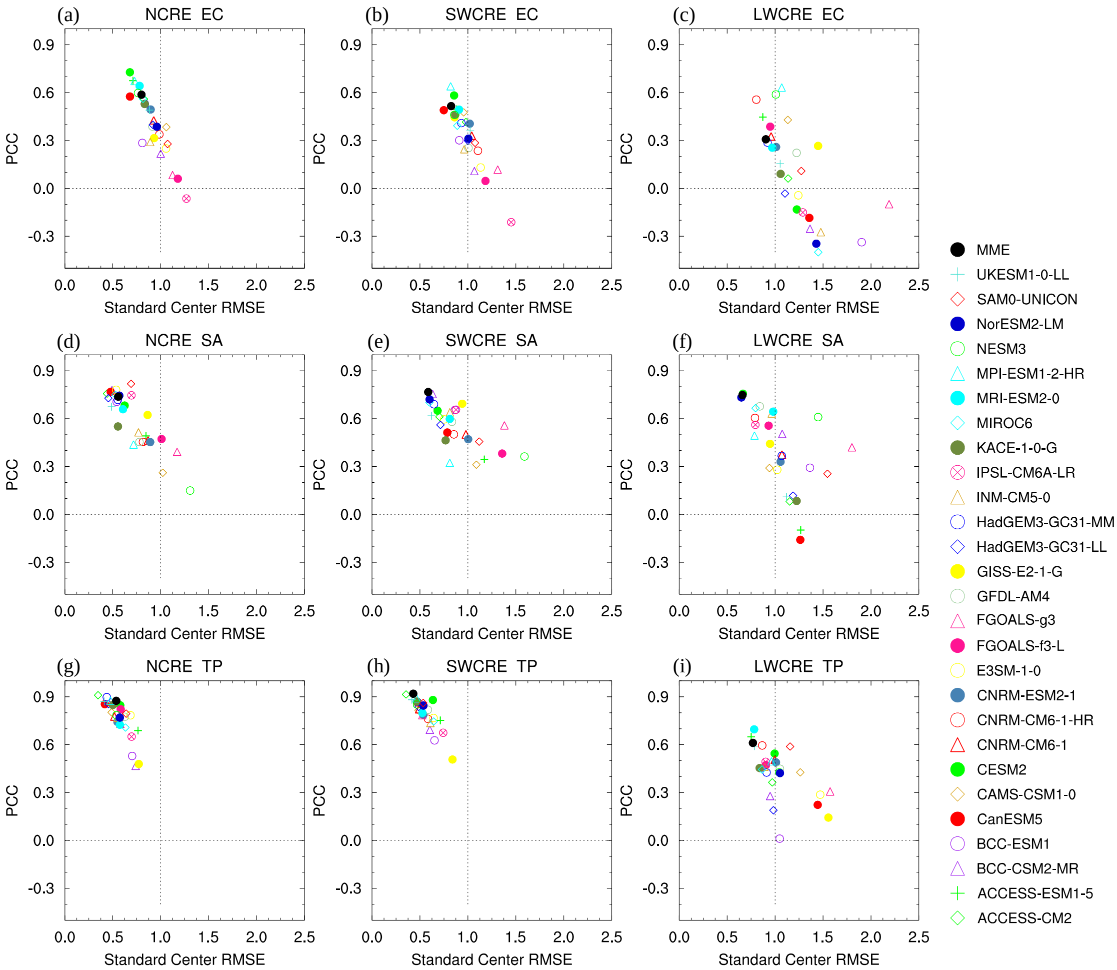

Figure 8. Pattern correlation coefficient and standard center RMSE between annual mean CMIP6 AMIP model and observational counterparts for NCRE, SWCRE and LWCRE over EC (Figures 8a, b, c), SA (Figures 8d, e, f) and the TP (Figures 8g, h, i).

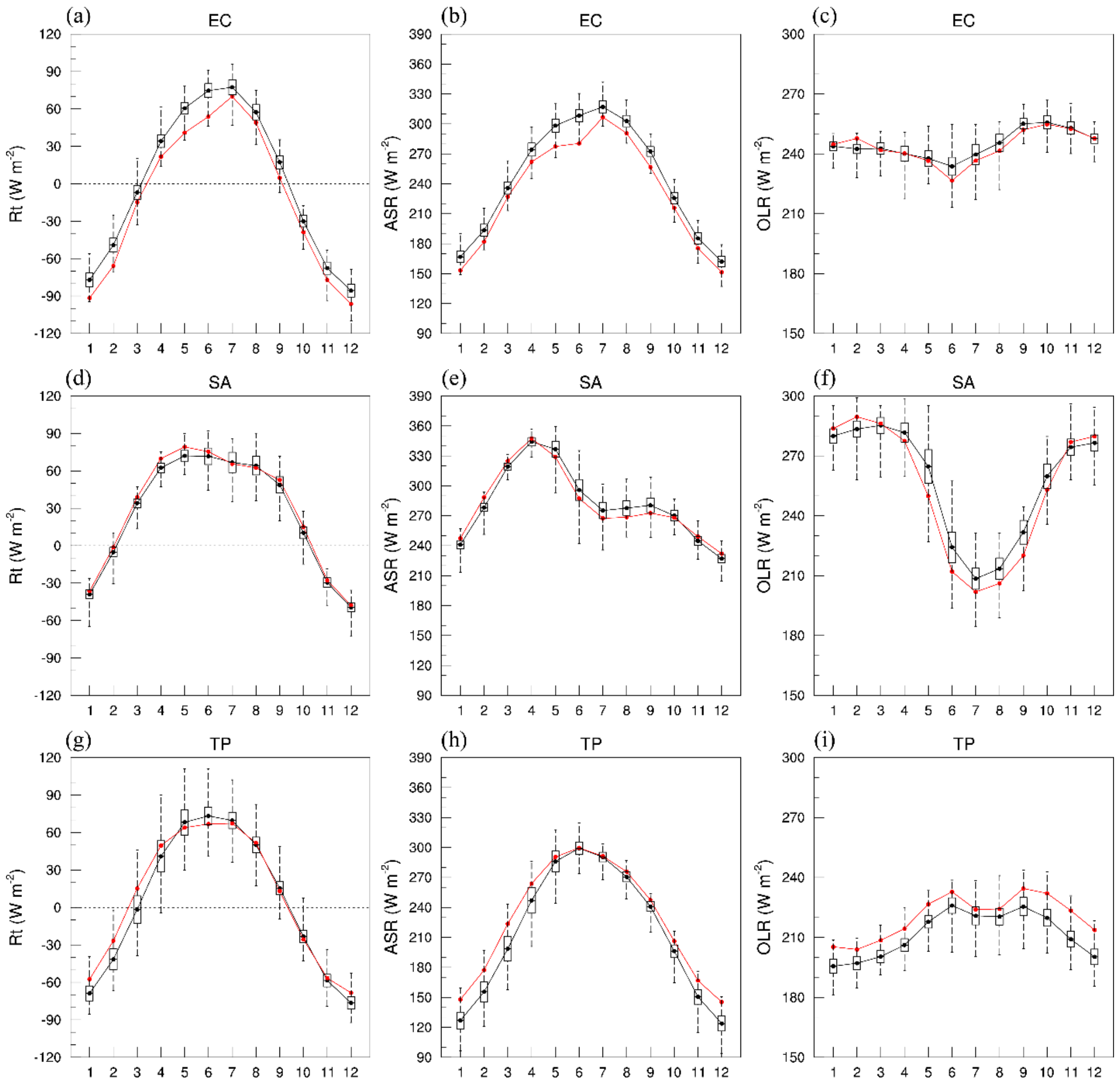

Figure 9. Seasonal cycles of simulated monthly and regional mean (a, d, and g) Rt, (b, e, and h) ASR, and (c, f, and i) OLR (unit: W m^{-2}) averaged over EC (Figures 9a–9c), SA (Figures 9d–9f), and the TP (Figures 9g–9i). The red and black solid lines denote the observation and MME, respectively. The black box indicates the standard deviation among the models. Here, the period is 2001-2014. The number at x axis is the month number.

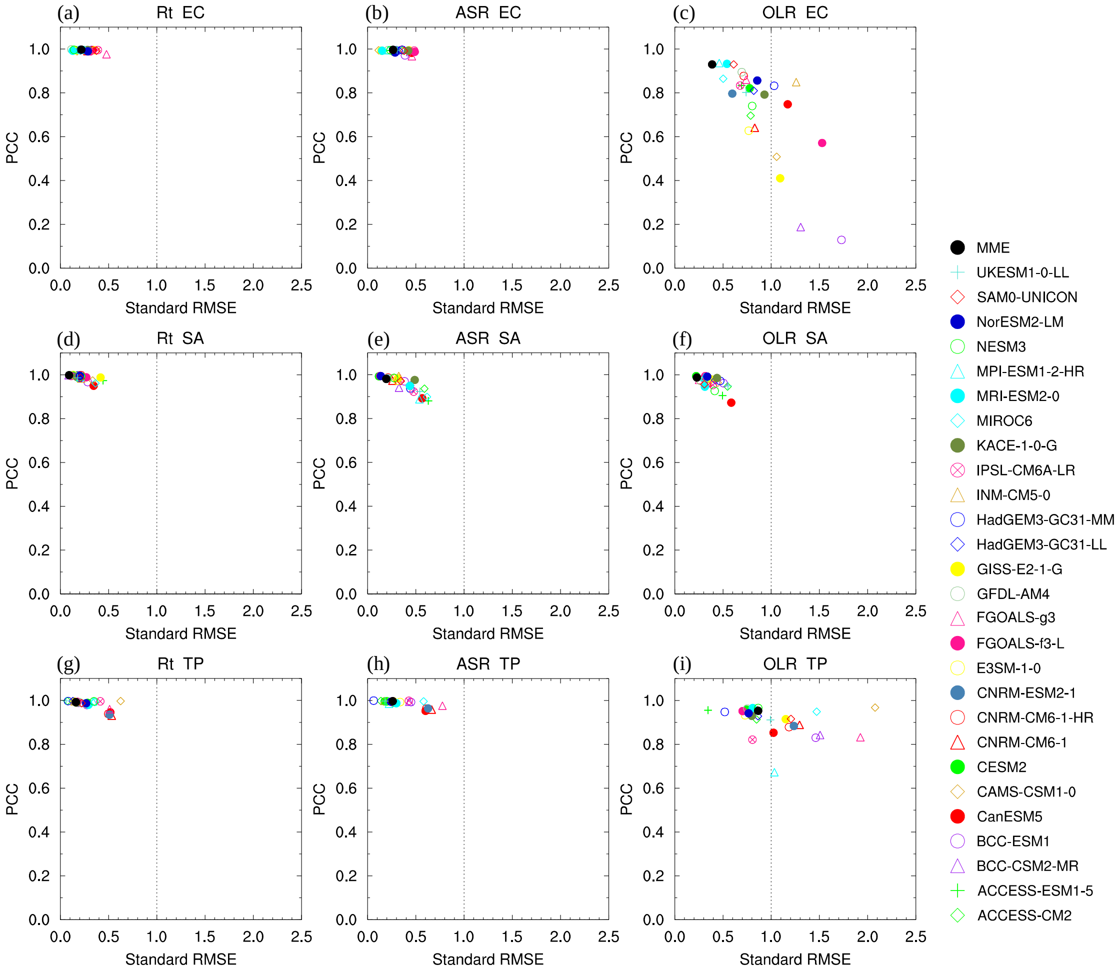

Figure 10. Pattern correlation coefficient and standard RMSE between annual cycles of CMIP6 AMIP model and observational counterparts for TOA Rt, ASR and OLR over EC (Figures 11a-11c), SA (Figures 11d-11f) and the TP (Figures 11g-11i) during 2001-2014. The center RMSE from a specific model is divided by the STD of observational counterpart.

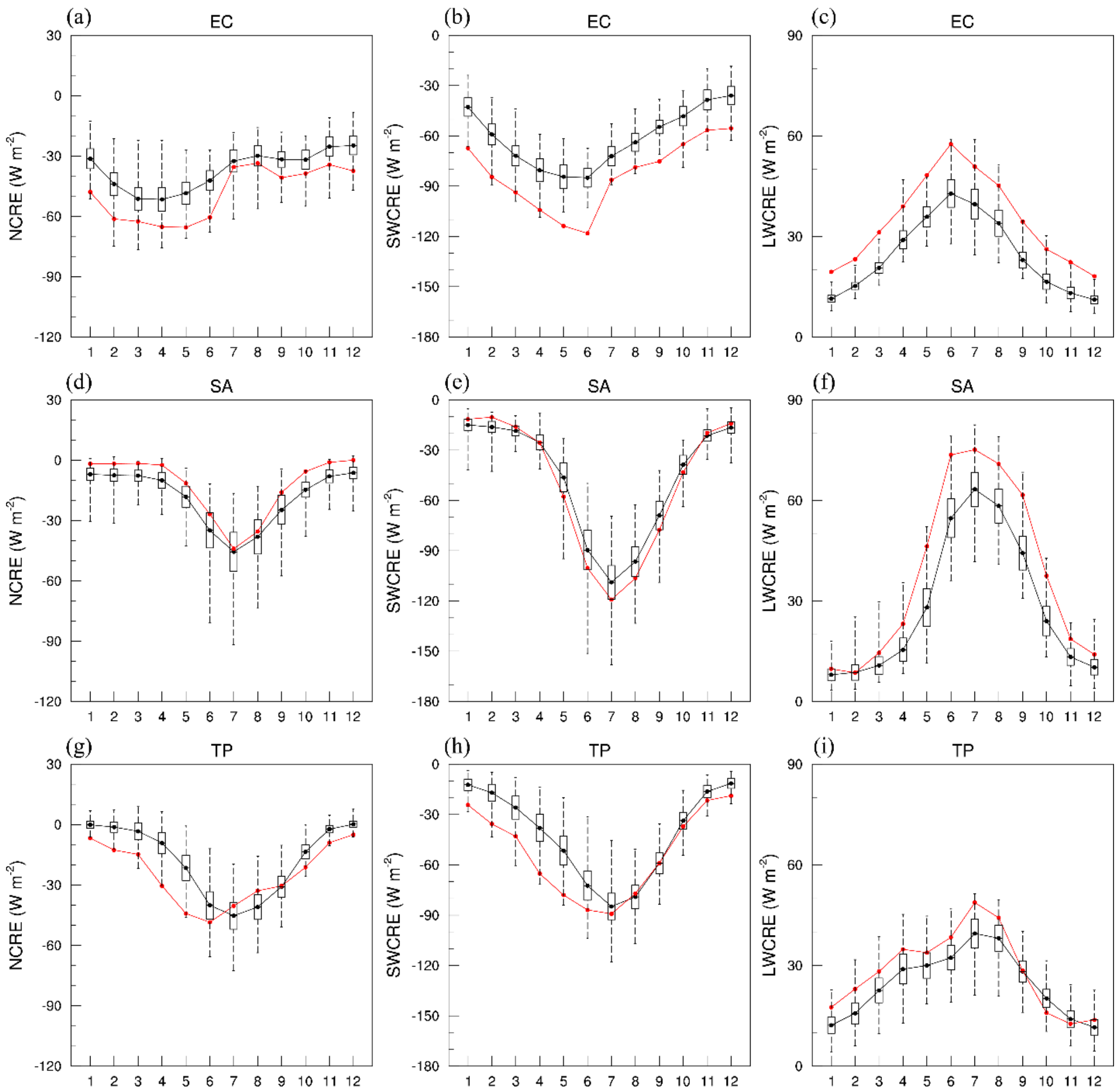

Figure 11. Seasonal cycles of simulated monthly and regional mean (a, d, and g) NCRE, (b, e, and h) SWCRE, and (c, f, and i) LWCRE (unit: W m^{-2}) averaged over EC (Figures 10a–10c), SA (Figures 10d–10f), and the TP (Figures 10g–10i). The red and black solid lines denote the observation and MME, respectively. The black box indicates the standard deviation among the models. The number at x axis is the month number.

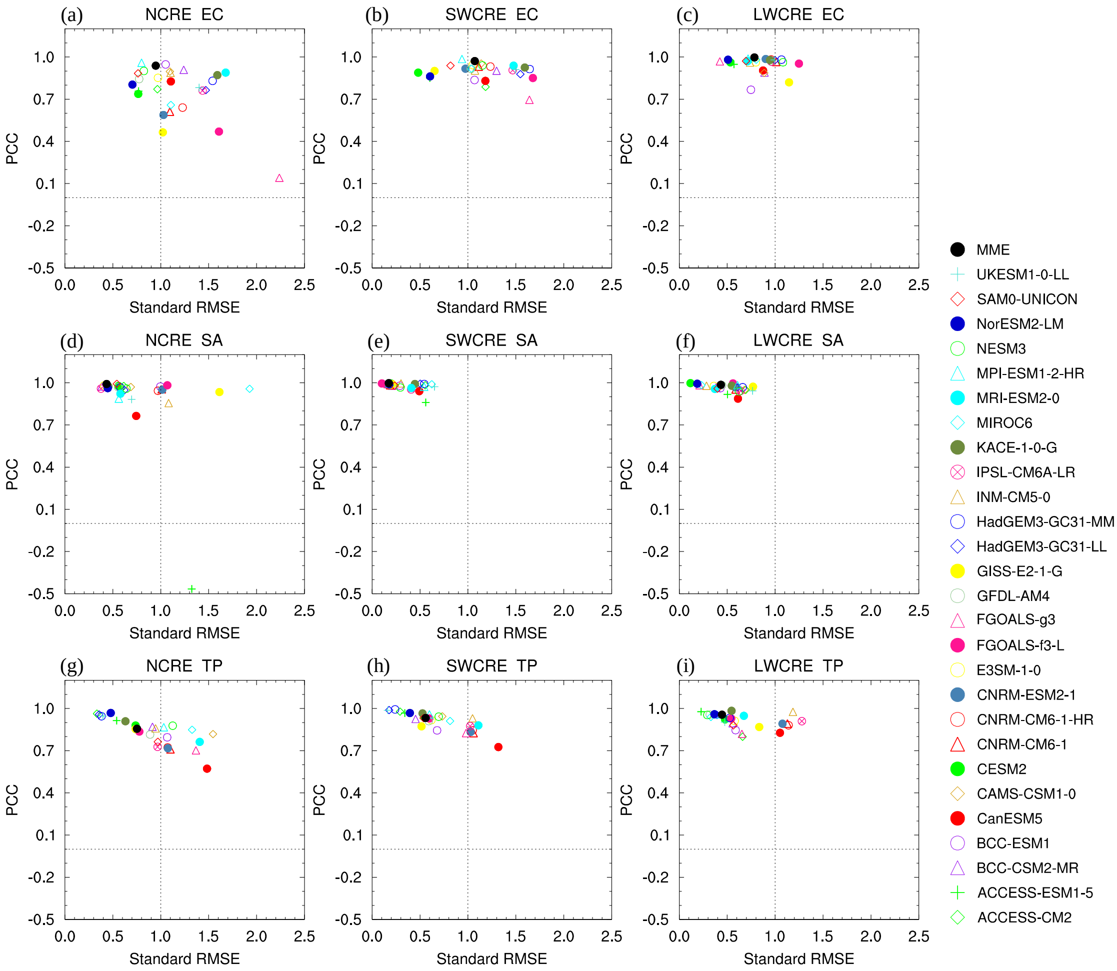

Figure 12. Pattern correlation coefficient and standard RMSE between annual cycles of CMIP6 AMIP model and observational counterparts for NCRE, SWCRE and LWCRE over EC (Figures 12a-12c), SA (Figures 12d-12f) and the TP (Figures 12g-12i) during 2001-2014. The center RMSE from a specific model is divided by the STD of observational counterpart.

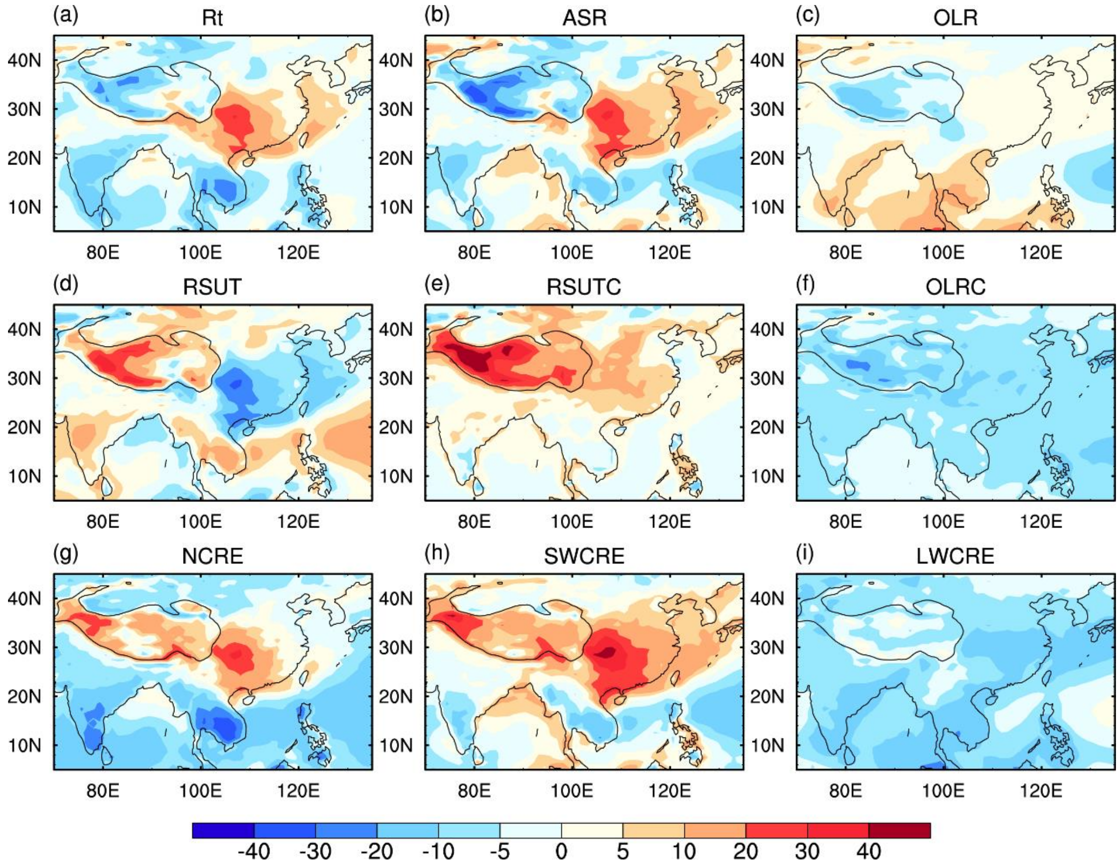

Figure 13. Distribution of annual mean biases of (a-i) Rt, ASR, OLR, RSUT, RSUTCS, OLRC, NCRE, SWCRE and LWCRE (unit: W m^{-2}) during 2001-2014 simulated from CMIP6 AMIP MME.

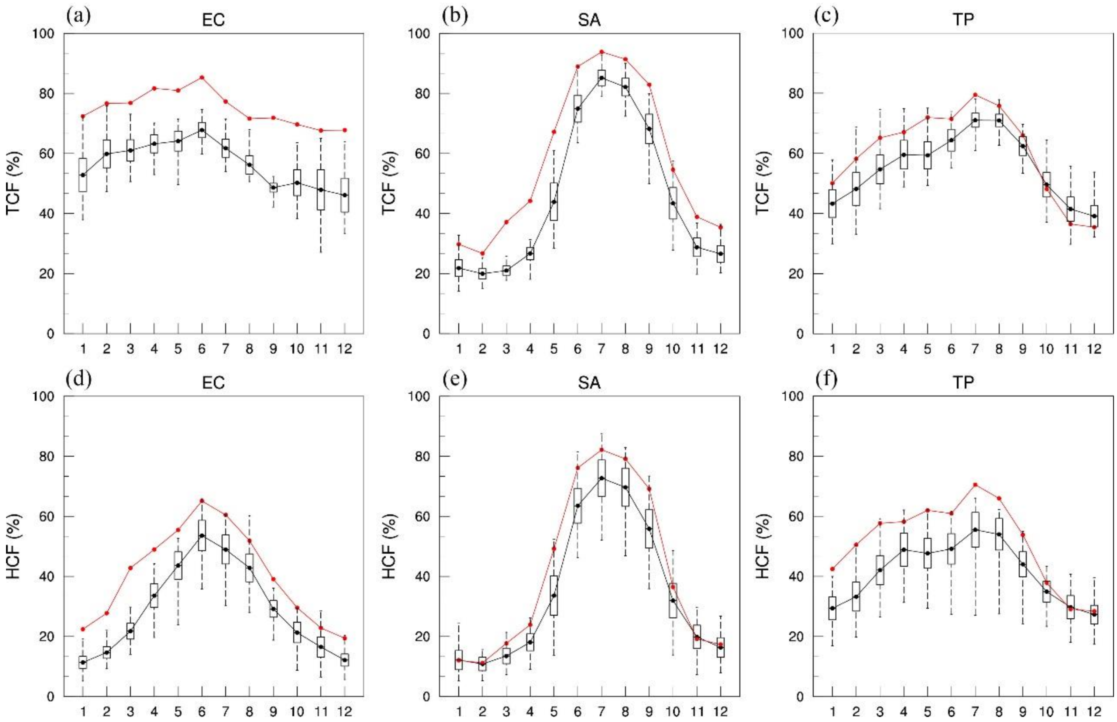

Figure 14. Seasonal cycles of monthly and regional mean (a, b, and c) TCF and (d, e, and f) HCF (unit: %) averaged over EC (Figures 14a, 14d), SA (Figures 14b, 14e), and the TP (Figures 14c, 14f) simulated by 9 CMIP6 models with satellite simulator output during 2007-2014. The red and black solid lines denote the observation and MME, respectively. The black box indicates the standard deviation among the models. The number at x axis is the month number.

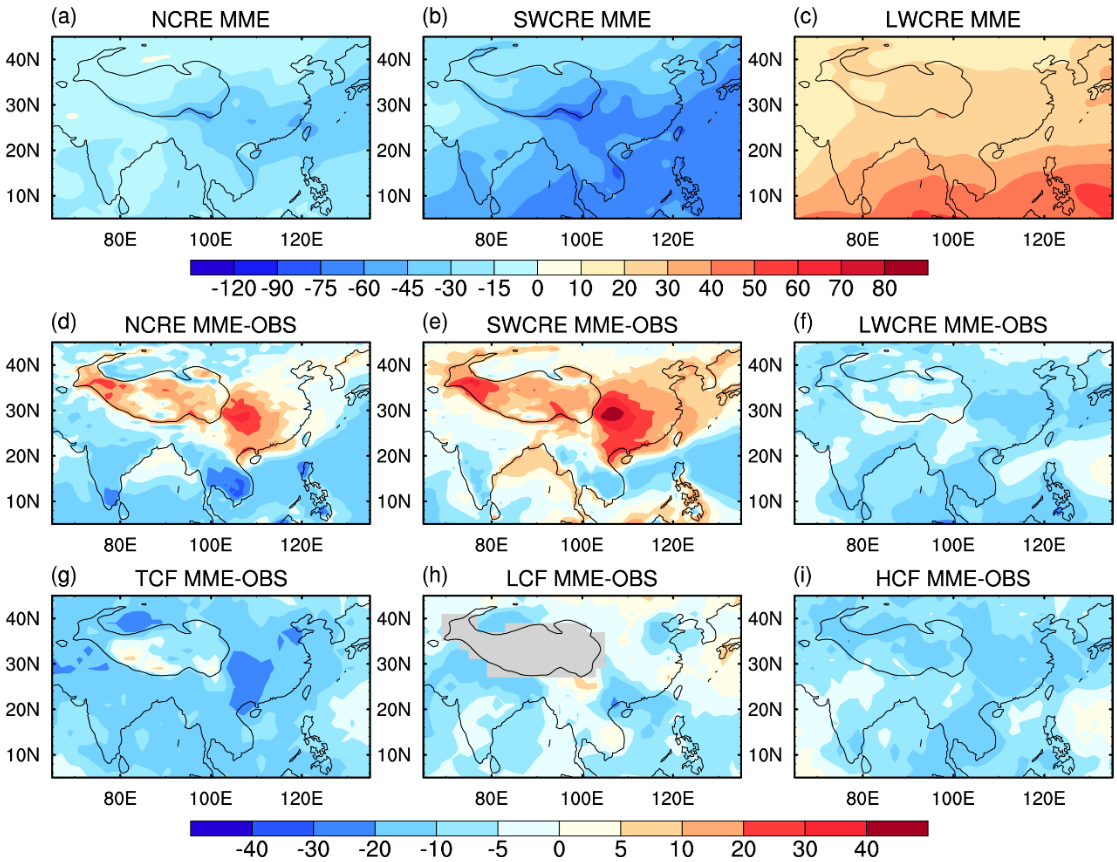

Figure 15. Distribution of (a-c) NCRE, SWCRE and LWCRE (W m^{-2}) in CMIP6 AMIP MME with satellite simulator output, and differences in (d-f) NCRE, SWCRE, LWCRE (W m^{-2}), TCF, LCF and HCF (%) between CMIP6 AMIP MME with satellite simulator output and GOCCP during 2007-2014.

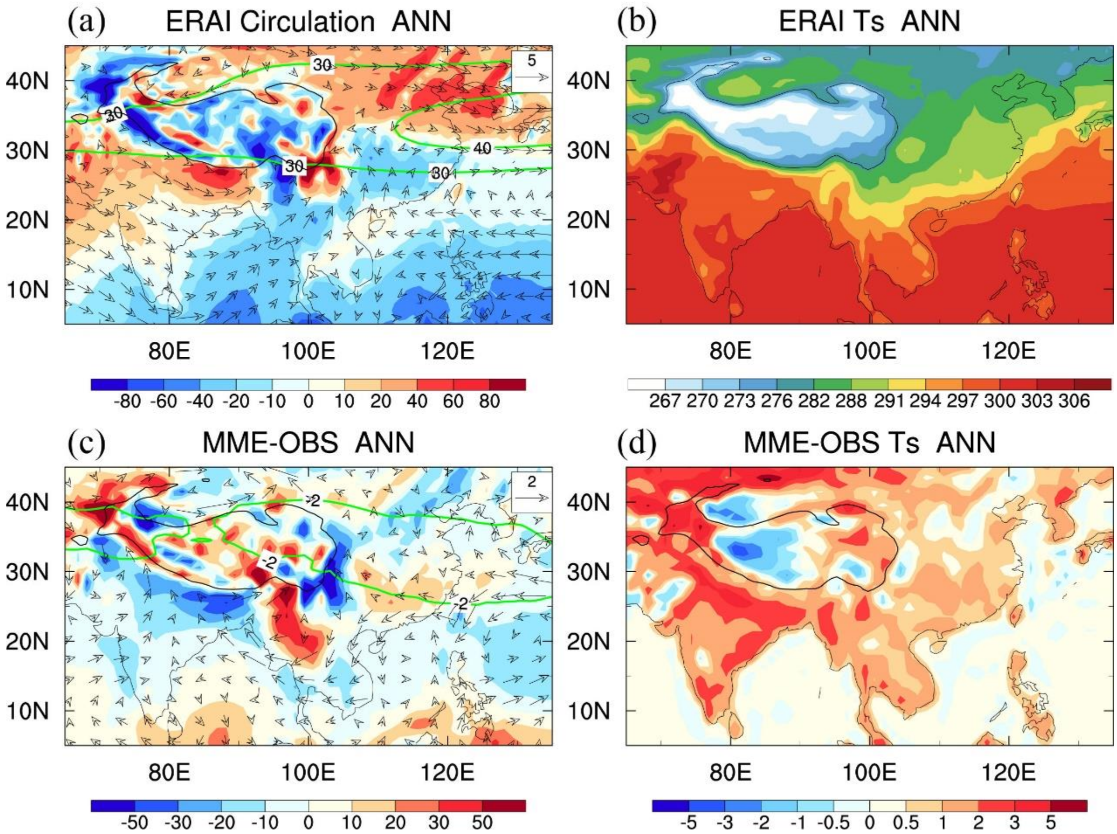

Figure 16. Distribution of (a-b) observational circulation condition and surface temperature (K), and (c-d) their differences between CMIP6 AMIP MME with satellite simulator output and the counterparts from ERA-Interim reanalysis during 2007-2014. In (a) and (c), black contours represent 200-hPa zonal wind speed (m s^{-1}) or its simulated biases relative to ERA-Interim analysis; arrows represent the 850-hPa wind field, with the graphic at top right showing an arrow corresponding to 5 (2) m s^{-1}; the black counter represents the TP topography (>3000m).